

1 **Transferability of a calibrated numerical model of rock avalanche run-out: application to 20 rock**
2 **avalanches on the Nuussuaq Peninsula, West Greenland**

3

4 **J. Benjamin^{1*}, N.J. Rosser¹, S.A. Dunning², R.J. Hardy¹, K. Kelfoun³, W. Szczuciński⁴**

5

6 ¹ Department of Geography and Institute of Hazard Risk and Resilience, Durham University, South Road,
7 Durham, DH1 3LE, UK.

8 ² School of Geography, Politics and Sociology, Newcastle University, Newcastle upon Tyne, UK.

9 ³ Laboratoire Magmas et Volcans, Université Blaise Pascal, Clermont-Ferrand, France.

10 ⁴ Institute of Geology, Adam Mickiewicz University in Poznań, Poznań, Poland.

11

12 *Corresponding author: Jessica Benjamin (jessica.benjamin@durham.ac.uk)

13

14 **Keywords**

15 Rock avalanches, Landslides, Numerical modelling, Calibration, Validation

16 **Abstract**

17

18 Long run-out rock avalanches are one of the most hazardous geomorphic processes, and risk
19 assessments of the potential threat they pose are often reliant on numerical modelling of their potential
20 run-out distance. The development of such models requires a thorough understanding of past flow
21 behaviour inferred from deposits emplaced by previous events. Despite this, few records exist of multiple
22 rock avalanches that occurred in conditions sufficiently consistent to develop a set of more generalised,
23 and hence transferrable, rules. We conduct field and imagery-based mapping and use numerical
24 modelling to investigate the emplacement of 20 adjacent rock avalanches on the southern flanks of the
25 Nuussuaq peninsula, West Greenland. The rock avalanches run out towards the Vaigat Strait, and are
26 sourced from a range of coastal mountains of relatively uniform geology. We calibrate a three-
27 dimensional continuum dynamic flow code, *VolcFlow*, with data from a modern, well-constrained event
28 that occurred at Paatuut (AD 2000). The best-fit model assumes a constant retarding stress with a
29 collisional stress coefficient, simulating run-out to within $\pm 0.3\%$ of that observed. This calibration was then
30 used to model the emplacement of deposits from five other neighbouring rock avalanches before
31 simulating the general characteristics of a further 14 rock avalanche deposits on simplified topography.
32 Our findings illustrate that a single calibration of *VolcFlow* can account for the observed deposit
33 morphology of a uniquely large collection of rock avalanche deposits, emplaced by a series of events
34 spanning a large volume range. Although the prevailing approach of tuning models to a specific case may
35 be useful for detailed back-analysis of that event, we show that more generally applied models, even
36 using a single pair of rheological parameters, can be used to model potential rock avalanches of varied
37 volumes in a region and, therefore, to assess the risks that they pose.

38 **1 Introduction**

39

40 Rock avalanches are large volume ($> 10^6 \text{ m}^3$), long run-out mass movements that exert a major and long-
41 lasting influence on landscapes by virtue of their ability to mobilise large volumes of material (Fischer *et*
42 *al.*, 2012), thereby limiting topographic relief and modulating sediment flux (Fort and Peulvast, 1995;
43 Korup, 2006). The secondary consequences of rock avalanches can often be more far-reaching and
44 severe than the events themselves. Far-field hazards can result from landslide dam breach (Korup, 2002)
45 and, where landslides run out into water, the direct impact and/or subsequent sub-aqueous slumping of
46 deposits can result in tsunami (Løvholt *et al.*, 2015; Gauthier *et al.*, 2017). The displacement waves
47 generated by rock avalanches that enter water bodies represent a major natural hazard for coastal
48 communities in the fjord regions of New Zealand (Dykstra, 2013), Norway (Olesen *et al.*, 2004; Böhme *et*
49 *al.*, 2015), British Columbia (Murty, 1979; Bornhold *et al.*, 2007), Alaska (Miller, 1960; Dufresne *et al.*,
50 2018), Chile (Sepúlveda and Serey, 2009), and, as seen recently, the deglaciated western margin of
51 Greenland (Dahl-Jensen *et al.*, 2004; Gauthier *et al.*, 2017). As well as pre-failure deformation
52 (Jaboyedoff *et al.*, 2011), seismic precursors have also been observed prior to large, tsunamigenic events
53 (for example, at Nuugaatsiaq, Greenland; Poli, 2017). Considerable emphasis has therefore been placed
54 on quantifying both the hazards and risks associated with actively deforming rock-slopes based on the
55 identification and monitoring of potential failures, estimation of rockslide properties, and modelling slope
56 stability and potential run-out using a combination of laboratory models and mathematical simulations
57 (Blikra *et al.*, 2005; Willenberg *et al.*, 2009; Gigli *et al.*, 2011).

58

59 The successful simulation of rock avalanche dynamics, potential run-out distance and tsunami generation
60 in fjord environments is contingent upon a thorough understanding of the flow dynamics inferred from
61 deposits left by previous events (Rickenmann, 2005). However, the poor preservation of deposits and the
62 need to map both terrestrial and subaqueous environments often confutes the validation of models
63 (Korup *et al.*, 2007). This is compounded by difficulties in simulating the complex behaviour of the rock
64 avalanche mass during both subaerial and subaqueous propagation, where successful modelling relies
65 upon selecting an appropriate approximation of the emplacement dynamics and rheology (Pirulli and

66 Mangeney, 2008). Recent modelling advances are progressing towards the simulation of complex two-
67 phase flows (Pudasaini and Krautblatter, 2014), with emphasis being placed on modelling the transition
68 from a terrestrial to subaqueous environment, and the displacement of water that results (Mergili *et al.*,
69 2017). These efforts are in their infancy and require extensive validation against well-constrained
70 prototypes rather than conceptual models of events (Mergili *et al.*, 2017). Single phase models have been
71 successfully used to model the terrestrial portion of rock avalanche run-out (Schleier *et al.*, 2017), and
72 can be used to provide the key characteristics for tsunami modelling. However, few records exist of
73 multiple rock avalanche events with boundary conditions sufficiently consistent to permit sensitivity
74 analysis to changes in key variables, such as volume. Most research involving numerical modelling of
75 rock avalanche run-out to date has therefore focussed on back analysing individual events, or events
76 defined by some larger grouping variable such as those that have occurred in a 'glacial environment'
77 (Sosio *et al.*, 2012). Models often need to be run with several differing rheologies in order to adequately
78 describe each of the key output variables such as velocity, run-out, flow width and depth. This approach
79 provides a broad envelope of rheological properties (Sosio *et al.*, 2008; 2012) that are usually unsuited to
80 predictive scenario modelling with acceptable errors, thereby precluding the development of a set of more
81 generalised rules for behaviour across rock avalanches in different settings (Evans *et al.*, 2006).

82
83 Here, we apply a single-phase modelling approach to a cluster of 20 rock avalanche deposits along the
84 Vaigat Strait, West Greenland. This presents the unique opportunity to model a large sample of adjacent
85 rock avalanches with well-preserved morphological and sedimentological records, and that are sourced
86 from a stretch of mountains of relatively uniform geology and (post-) glacial history. The rock avalanche
87 and corresponding tsunami at Paatuut (AD 2000) is well-documented (Pedersen *et al.*, 2002; Dahl-
88 Jensen *et al.*, 2004), and represents an important opportunity for calibration of a numerical model by
89 back-analysis. As the geomorphological and geological conditions are relatively uniform across this
90 region, we first use a case-specific calibration to investigate the ability of several commonly invoked
91 rheologies to reproduce the kinematics and deposit geometry of the Paatuut event. The best-fit
92 rheological model is then used to simulate a wider set of event deposits in Vaigat to establish its ability to
93 be used for predictive modelling.

94 **2 Study site**

95

96 Located in the Disko Bugt region of central West Greenland, the northern coast of the Vaigat Strait offers
97 a unique geological setting that has generated a cluster of 20 rock avalanche deposits (Figure 1;
98 Pedersen *et al.*, 2002). The stratigraphic succession comprises a series of hyaloclastite breccias and
99 subaerial lava flows of the Palaeocene Vaigat and Maligât formations that overlie sedimentary rocks,
100 including sandstones, mudstones and coal seams, of the Cretaceous Atane and the Danian Quikavsak
101 formations (Pedersen and Pulvertaft, 1992; Dam and Sønderholm, 1998). These conditions are thought
102 to be particularly favourable for the generation of rock avalanches along Vaigat's coastal slopes,
103 especially where erosion exposes the underlying soft units (Strom, 2004). Given that active faulting in
104 Vaigat is minimal (Voss *et al.*, 2007), the rock avalanches are thought to have been triggered by
105 progressive deformation of the valley side-walls in response to glacial over-steepening (Pedersen *et al.*,
106 2002). Climatic controls are considered to have acted as a direct trigger of the 21 November 2000
107 Paatuut rock avalanche, where a particularly deep active layer of permafrost was present (Buchwał *et al.*,
108 2015) and fluctuations in air temperature in the days prior to the event drove the repeated melting and
109 refreezing of water in surface cracks (Dahl-Jensen *et al.*, 2004).

110

111 The 20 onshore rock avalanche deposits are clearly identifiable from their geomorphological expression
112 (Figures 2 and 3). Source areas range from conspicuous, structurally-controlled hollows above deposits
113 (Figure 2a), to near-vertical faces with source areas that are more difficult to define. The deposits are
114 characterised by variable volumes ($2 \times 10^6 - 90 \times 10^6 \text{ m}^3$), run-out (1,270 – 4,383 m) and stalling
115 characteristics, with some halting on or above a topographic bench or an alluvial fan (RA 2 – 5; Figure
116 2b), some running out to sea level (RA 8 and RA 9) and some emplaced into the fjord, generating
117 tsunamis (RA 1 and RA 16; Figure 2c). The deposits are distinct from the well-studied rock glaciers on
118 Disko Island, which lies on the opposite side of the strait (Humlum, 2000). Some deposits are relatively
119 younger with sharper, more well-defined morphologies, steep termini (Figure 2d) and a carapace of
120 coarse clastic material (Figure 2e; as observed in Crosta *et al.*, 2007; Dufresne *et al.*, 2016; Dufresne and
121 Dunning, 2017). Many of them tend to consist of a complex of partially overlapping and anastomosing

122 lobes, with extensive fields of small, conical mounds ('molards'; Figure 2f) and longitudinal pressure
123 ridges. These form (sub-) parallel to the flow direction, often standing up to tens of metres high, and have
124 been observed on the surfaces of many rock avalanche deposits. These observations, as well as the
125 results of laboratory experiments, have been used to suggest that emplacement velocity, bulk/material
126 density, and frictional behaviour combine to control the degree to which prominent longitudinal features
127 form (Dufresne and Davies, 2009). Their occurrence has also been attributed to the incorporation of ice
128 into the flow (Huggel *et al.*, 2005). Notably, given the proximity of many of the deposits to alluvial fans that
129 undergo periodic debris-flow activity, it is possible that older rock avalanche deposits exist in the area that
130 have not been recognised due to reworking.

131
132 The deposits are younger than 10 ka, and are likely to have been emplaced since *ca.* 3 ka based on their
133 relationship with various local Holocene sea level markers (Long *et al.*, 2011). They contain a total of >
134 $350 \times 10^6 \text{ m}^3$ of material along some 25 km of coastline, equivalent to a *ca.* 2 m drape of sediment across
135 the entire landscape when a 5 km wide slope is assumed. Assuming an age of < 3 ka, the volume of
136 material contained in these deposits is equivalent to *ca.* 4 mm yr⁻¹ of average horizontal rockwall retreat.
137 They are well preserved but weathered to varying degrees, suggesting either variable ages or
138 significantly different weathering rates, although we consider this unlikely given the similarity of source
139 lithology and near horizontal bedding along the coast. The surface morphologies of the deposits support a
140 rapid rock avalanche emplacement process (Dufresne and Davies, 2009); the margins are steep,
141 longitudinal boulder ridges and lobate flow units are present, and distal margins show bulldozing of
142 underlying sediments (Figures 2 and 3).

143

144 **3 Methods**

145

146 We have modelled the onshore portion of 20 rock avalanche deposits (Figure 1) that have previously
147 been documented by Pedersen *et al.* (2002). The geometric characteristics of the deposits are
148 summarised in Table S1, and details of the mapping and GIS-based analysis undertaken are given in
149 Text S1.

150 3.1 Numerical flow code

151

152 The rock avalanche motion is modelled using the geophysical mass flow code *VolcFlow* (Kelfoun and
153 Druitt, 2005). *VolcFlow* has been tested on a number of debris avalanches and pyroclastic flow events,
154 successfully simulating avalanche run-out and emplacement dynamics in a number of settings (Kelfoun
155 and Druitt, 2005; Kelfoun *et al.*, 2008; 2009; 2010; Giachetti *et al.*, 2011; Kelfoun, 2011; Paris *et al.*, 2011;
156 Charbonnier and Gertisser, 2012; Dondin *et al.*, 2012; Giachetti *et al.*, 2012; 2013; Manzella *et al.*, 2016;
157 Kelfoun, 2017; Kelfoun *et al.*, 2017). As with many other continuum dynamic models used for simulating
158 rock avalanche propagation (Savage and Hutter, 1989; Iverson *et al.*, 1997; McDougall and Hungr, 2004),
159 *VolcFlow* is governed by a continuity and momentum equation based on the Saint-Venant equations of
160 shallow flow. These are derived by integrating the Navier-Stokes equations with respect to flow depth in a
161 procedure known as depth-averaging (Hungr, 1995). The model therefore constitutes a 2.5D
162 representation and assumes that stresses increase linearly with depth, neglecting shear stresses in the
163 depth direction. It is also assumed that the depth of the flowing mass varies gradually and is small in
164 relation to its overall extent, which is a classical shallow flow assumption of hydrodynamics (Chow, 1959).

165

166 The governing equations in *VolcFlow* are solved using a shock-capturing, finite difference numerical
167 method based on a single upwind Eulerian scheme (Kelfoun and Druitt, 2005). With reference to a
168 topography-linked coordinate system, where the flow depth, h (m) over time, t (s) is measured normal to
169 the sliding surface and x and y are parallel to it, the depth-averaged equations of mass (Eq. 1) and
170 momentum (Eq. 2 and Eq. 3) conservation are:

171

$$172 \quad \frac{\partial h}{\partial t} + \frac{\partial}{\partial x}(hv_x) + \frac{\partial}{\partial y} = 0 \quad (1)$$

$$173 \quad \frac{\partial}{\partial t}(hv_x) + \frac{\partial}{\partial x}(hv_x^2) + \frac{\partial}{\partial y}(hv_x v_y) = gh \sin \alpha_x - \frac{1}{2} k_{act/pass} \frac{\partial}{\partial x}(gh^2 \cos \alpha) + \frac{\tau_x}{\rho} \quad (2)$$

$$174 \quad \frac{\partial}{\partial t}(hv_y) + \frac{\partial}{\partial x}(hv_y v_x) + \frac{\partial}{\partial y}(hv_y^2) = gh \sin \alpha_y - \frac{1}{2} k_{act/pass} \frac{\partial}{\partial y}(gh^2 \cos \alpha) + \frac{\tau_y}{\rho} \quad (3)$$

175

176 where v_x and v_y are the x and y components of the flow velocity (m s^{-1}); α is the local ground slope ($^\circ$); τ is
177 the basal shear stress ($\text{kg m}^{-1} \text{s}^{-2}$); ρ is the bulk density of both the landslide and the path material (kg m^{-3});
178 g is the acceleration due to gravity (9.81 m s^{-2}); and $k_{act/pass}$ is the earth pressure coefficient, which is the
179 ratio of ground-parallel to ground-normal stress.

180
181 The motion of rock avalanches in models is often governed by simple rheological laws that can vary
182 internally and/or along the path of motion (McDougall, 2006). Depth-averaging allows the rheology to be
183 represented as a single term that expresses the frictional forces occurring at the base of the flow (Luna *et al.*,
184 2010). A number of rheological laws have been invoked for the simulation of rock avalanches, the
185 mathematical expressions for which solve for the basal shear stress as a function of flow depth, density,
186 mean flow velocity and the relevant rheological parameters. In *VolcFlow*, we define the basal rheology
187 using a frictional (one or two angle), Voellmy or a plastic rheology, each of which are well-established for
188 simulating rock avalanche propagation (Evans *et al.*, 1989; Chen and Lee, 2000; Crosta *et al.*, 2004;
189 Hungr and Evans, 2004; McDougall and Hungr, 2004; Sosio *et al.*, 2008; 2012). The choice of rheology is
190 often dictated by the output variable of interest, such as the overall runout extent or velocity. No single
191 rheological model has proven to model definitively all output variables of interest, partially due to the
192 issues of tuned back analyses versus generality, which we address here. We present the mathematical
193 expressions of τ in depth-averaged form, as derived by Kelfoun (2011), where the terms in **bold** are to be
194 defined in *VolcFlow* depending on the chosen rheology.

195
196 Frictional basal resistance assumes that the basal shear stress is a function of the effective bed normal
197 stress at the flow base and the friction angle, φ_{bed} , between the flow and the underlying topography. The
198 equation defining the basal shear stress for a frictional flow is:

199
201
$$\tau = \rho h \left(g \cos \alpha + \frac{u^2}{r} \right) \tan \boldsymbol{\varphi}_{bed} \frac{u}{\|u\|} \quad (4)$$

200
202 where u is the depth-averaged flow velocity (m s^{-1}) and r the slope curvature (-). In a one angle frictional

203 model, the internal angle of friction of the flowing material, φ_{int} , is equal to φ_{bed} and the internal stresses
 204 are considered to be isotropic. In *VolcFlow*, the earth pressure coefficient, $k_{act/pass}$, is therefore equal to 1.
 205 In a two-equation frictional law, φ_{int} can differ from φ_{bed} , thereby acting on the earth pressure coefficient
 206 and modifying the stresses induced by the pressure gradient. This allows for strain-dependent,
 207 anisotropic internal stresses that arise due to the 3D deformation of material during topographically
 208 steered or restricted flow (McDougall and Hungr, 2004). If the internal behaviour of the sliding mass is
 209 frictional, then:

$$211 \quad k_{act/pass} = 2 \left(\frac{1 \pm \sqrt{1 - \cos^2 \varphi_{int} (1 + \tan^2 \varphi_{bed})}}{\cos^2 \varphi_{int}} \right) - 1 \quad (5)$$

212
 213 The minimum and maximum values of the stress coefficients occur when the flow is extensional (active)
 214 and compressional (passive), respectively.

215
 216 A number of rheological models invoke a velocity-dependent term (Wadge *et al.*, 1998). For example, the
 217 Voellmy rheology describes the total resistance as the sum of a frictional term, φ_{bed} , and a collisional
 218 stress coefficient, ξ (dimensionless), such that:

$$219 \quad \tau = \rho h \left(g \cos \alpha + \frac{u^2}{r} \right) \tan \varphi_{bed} \frac{u}{\|u\|} + \xi \rho \|u\| \times u \quad (6)$$

220
 221 The turbulence parameter thereby accounts for all possible sources of velocity-dependent resistance,
 222 representing the effect of turbulence and/or collisions during motion (Hutter and Nohguchi, 1990; Evans
 223 *et al.*, 2001).

224
 225
 226 A plastic rheology is often used to describe the pseudo-static motion of liquefied soils, which remain at
 227 rest while the applied shear stress is below a threshold yield stress. Once movement begins, the shear
 228 stress exerted by the material is constant, irrespective of its thickness and/or its velocity (Dade and
 229 Huppert, 1998). The basal shear stress is assumed to be equal to a constant shear strength, τ_0 :

231
$$\tau = \tau_0 \frac{u}{\|u\|} \quad (7)$$

230

232 The velocity and run-out of a flow modelled using the plastic rheology can also be moderated by adding a
233 collisional stress coefficient, ξ .

234

236
$$\tau = \tau_0 \frac{u}{\|u\|} + \xi \rho \|u\| \times u \quad (8)$$

235

237 Following deposition, deposits formed using a plastic rheology remain plastic at rest, even when
238 deposited on steep slopes.

239

240 **3.2 Model calibration**

241

242 The model was first calibrated by back analysis of the rock avalanche at Paatuut (RA 1), shown in Figure
243 4a. The rock avalanche initiated at *ca.* 1,400 m above sea level, detaching $> 90 \times 10^6 \text{ m}^3$ of basalt from
244 two steep (*ca.* 60°) release surfaces. Both the initial collapse and the propagation of the rock avalanche
245 were captured at three broadband seismic stations, providing constraints on flow velocity and event
246 duration (Pedersen *et al.*, 2002). The rock avalanche ran out into the Vaigat Strait at $140 - 200 \text{ km h}^{-1}$,
247 where part of the submerged deposit toe then slumped into the sea. The collapse generated a tsunami
248 with a run-up of *ca.* 50 m on the coast adjacent to Paatuut (Dahl-Jensen *et al.*, 2004) and over 10 m on
249 the opposite shoreline, 20 km away (Szczeniński *et al.*, 2012). We model the rock avalanche on available
250 25 m topography, the details of which are provided in *Section 3.4*.

251

252 In total, 41 models were run with the aim of reproducing: (i) the maximum run-out distance, (ii) the
253 kinematics of the event (maximum flow velocity and duration of emplacement), and (iii) the first-order
254 morphology of the subaerial rock avalanche deposit (Table 1). The rheological parameters, φ_{bed} , φ_{int} , ξ
255 and τ_0 , were selected using a systematic approach and iteratively adjusted in fixed intervals for each
256 rheology until the model outputs converged as closely as possible with the chosen criteria, which were

257 used as a means of evaluating the empirical adequacy of the model (Oreskes *et al.*, 1994). For the
258 Voellmy rheology, φ_{bed} was selected first as to reach the observed distal end of deposition, followed by
259 the adjustment of ξ , which controls the proximal end limit of deposition and the flow velocity. For the
260 plastic rheology with a collisional stress, τ_0 was selected first as to reach the observed distal end of
261 deposition, followed by the adjustment of ξ . Where possible, the calibration procedure was undertaken in
262 keeping with the range of values commonly found in the literature on natural subaerial rock avalanches
263 (Sosio *et al.*, 2008; Giachetti *et al.*, 2011; Kelfoun, 2011).

264
265 The assumptions required to run and evaluate the Paatuut case are supported by information available
266 from the literature (Pedersen *et al.*, 2002; Dahl-Jensen *et al.*, 2004), as well as measurements made
267 during a GIS-based analysis of the deposit (Table 1). These include a number of commonly recorded
268 characteristics, as well as the hypsometric integral of the deposit. The hypsometric integral is a non-
269 dimensional measure of the proportion of a landform above a given elevation and here constitutes an
270 important criterion for assessing model performance (Willgoose and Hancock, 1998). The increase in
271 volume due to bulking or fragmentation processes is not simulated by the code. We therefore increased
272 the source volume by 25%, replicating the approach of Sosio *et al.* (2012) and Moore *et al.* (2017), in
273 order to include the volume increase during rock avalanche propagation due to generation of void spaces
274 and dilatation (Voight *et al.*, 1983). All simulations assumed a single collapse of *ca.* $90 \times 10^6 \text{ m}^3$ of basalt
275 ($\rho = 2,150 \text{ kg m}^{-3}$) that propagated across dry topography and were ended when the velocity of the flow
276 reached 0 m s^{-1} . The mass was initially forced to slide over the plateau (*ca.* 750 m in length) as a block
277 before cohesion of the failed mass decreased as it began to flow down-valley. This capability was
278 enabled to simulate the early sliding phase of the rock avalanche (Voight and Faust, 1982; Kelfoun,
279 2014), which is thought to have initiated as an intact rockfall/slide (Dahl-Jensen *et al.*, 2004). This initially
280 coherent stage has greatly improved back-analyses of similar rock avalanches, with little parameter
281 sensitivity (Aaron and Hungr, 2016; Aaron *et al.*, 2017). Measures of entrainment, such as spatial
282 patterns of eroded depths and the downslope lag rate, have not been made for the Paatuut event. These
283 processes were not simulated as they could not be adequately parametrised, nor reasonably generalised
284 across all events in our database of rock avalanches.

285 **3.3 Application to other rock avalanches**

286

287 Numerical simulations using *VolcFlow* were performed for the remaining 19 rock avalanches using the
288 best-fit rheological parameters obtained by back-analysis of the Paatuut event (Figures 4 and 5). A
289 detailed description of these events is given in Text S2. Five rock avalanches were also simulated across
290 2.5D terrain, while the last 14 were modelled on simplified 2.5D terrain, the generation of which is
291 described in *Section 3.4*. The rock avalanches modelled in full 2.5D were chosen based on their clear
292 morphological expression, and are representative of a range of event types occurring in Vaigat. They
293 include, with deposit numbers in parentheses relating to Figure 1c: (i) an event that ran out to sea-level
294 and generated a tsunami (RA 16), (ii) an event that ran out to sea-level and stalled (RA 14), (iii) an event
295 that stalled on an alluvial fan (RA 10), (iv) and two events that stalled on and above a major topographic
296 bench, respectively (RA 4 and RA 2). Those remaining models, run across terrain that was uniform
297 across slope but variable downslope, provide a test-bed for assessing the ability of the model to simulate
298 run-out on a reduced level of topographic complexity. As such, we explore the value of modelling on
299 lower resolution topography, which may be more common when looking to assess rock avalanche hazard
300 at larger scales, more quickly.

301

302 **3.4 Topographic data**

303

304 The Paatuut rock avalanche deposit and local topography was characterised using 10 m resolution pre-
305 and post-event DEMs generated by the Geological Survey of Denmark and Greenland (GEUS). The
306 DEMs were downsampled by cubic convolution to 25 m in order to remain consistent with other available
307 topographic data for the area. Estimates of the magnitude and spatial distribution of erosion and
308 deposition at Paatuut were derived by differencing the DEMs. The post-collapse scar elevations were
309 then extracted from the 2001 DEM and mosaicked onto the 1985 DEM to derive the topography of the
310 sliding surface for input into *VolcFlow*. Vertical erosional depths were converted into depths normal to the
311 ground using the cosine of the local slope. A schematic diagram of this procedure is provided in Figure
312 S1.

313

314 All other cases were modelled using the 25 m Greenland Ice Mapping Project DEM (Howat *et al.*, 2014).

315 For the events modelled in full 2.5D, we reconstruct pre-failure topographies by modifying the original

316 terrain data in the source and path areas according to event descriptions and morphological evidence;

317 this includes field observations as well as available airborne and satellite data. For the events modelled

318 using simplified 2.5D terrain, this was generated by extruding a long single profile of each rock avalanche

319 in a uniform manner across-contour at 25 m intervals; each value of Y (across slope distance) therefore

320 had identical values of X (downslope distance) and Z (height). This was deemed appropriate given the

321 open and largely consistent slope profile form on this coastal slope.

322

323 **4 Modelling results**

324

325 We first present the results of the Paatuut model calibration. Five rheologies were tested to simulate the

326 propagation of the rock avalanche. The parameters and results of the best-fit simulation for each rheology

327 are summarised in Table 2. In *Section 4.2*, we consider the ability of best-fit parameters to accurately

328 simulate the other events in Vaigat, including 14 events simulated across simplified terrain.

329

330 **4.1 Rheological calibration**

331

332 In all simulations using a one angle frictional rheology, the velocity of the source mass following collapse

333 was relatively slow (*ca.* 10 m s⁻¹) as it flowed across a low gradient (*ca.* 6 – 7°) plateau at the base of the

334 escarpment. At greater basal frictional angles (17 – 20°) the mass accumulated over a very limited

335 distance, with much of the source mass remaining stalled on the plateau (Figure 6a). These

336 parameterisations therefore underestimate the known average velocity of the rock avalanche. The run-out

337 is more satisfactorily simulated using lower basal friction angles ($\varphi_{bed} = 13 - 15^\circ$), with the best-fit model

338 achieving within $\pm 3\%$ of the observed run-out ($\varphi_{bed} = 14^\circ$; Table 2). For these cases, a higher proportion

339 of the mass left the source area and flowed through the gullies in the Atane Formation before forming a

340 sheet-like deposit with a rounded frontal lobe and gentle downstream slopes. Although the best-fit

341 frictional model is successful in reproducing the run-out at Paatuut, it is unable to sufficiently replicate the
342 deposit morphology and the known kinematics of the event, overestimating the maximum velocity (+59%)
343 and duration of emplacement (+130%), and underestimating the average velocity (-31%) of the flow
344 (Table 2).

345
346 Using a two angle frictional rheology, the flowing mass behaved similarly to the previous set of
347 simulations. However, as $\varphi_{int} > \varphi_{bed}$, the deposits were emplaced closer to the source, with a small
348 component forming a thickening wedge at the distal end (Figure 6b). Although the best-fit model is able to
349 simulate the event to within $\pm 2\%$ of the observed run-out ($\varphi_{bed} = 12^\circ$, $\varphi_{int} = 30^\circ$), the simulated flows were
350 emplaced slowly (+211%), and the run-out extent and spreading was only achieved by a fraction of the
351 failed mass due to strong spreading of the frontal wedge by inertia. Although several of the flows are able
352 to adequately reproduce the extent of run-out at Paatuut, combining a realistic internal friction angle (30°
353 or 35°) with any commonly-used basal friction angle ($10 - 15^\circ$) fails to reproduce the initial collapse of the
354 source mass, the kinematics of the event, or the overall morphology of the resultant deposit.

355
356 The Voellmy rheology adds a collisional stress coefficient (ξ), which depends on the square of the flow
357 velocity, to the frictional model. The addition of ξ incorporates the effects of simulated turbulence and/or
358 collisions within the flow, reducing its maximum velocity and providing a better fit than that simulated by
359 either of the frictional laws (-14%; Table 2). The lower inertia allows the mass to accumulate closer to the
360 point where the topographic slope equals φ_{bed} (Figure 6c). A greater proportion of the collapsed mass
361 was therefore able to flow out of the source area, through the gullies in the Atane Formation, and then out
362 onto the alluvial fan below. The deposits therefore accumulated at greater thicknesses in the medial and
363 distal reaches, which is in agreement with field observations at Paatuut. The hypsometry of deposits
364 modelled using a Voellmy rheology converges with the morphology of the observed deposit. Although the
365 best-fit model fails to simulate the extent of the run-out as closely as the frictional models (-6%; $\varphi_{bed} =$
366 13° , $\xi = 0.01$), it can better simulate the distribution of the resultant deposit and can more accurately
367 reproduce the horizontal displacement of the centre of mass (-20%), maximum flow velocity (-14%) and
368 average deposit thickness (-11%; Table 2).

369

370 The plastic rheology assumes a constant retarding stress, τ_0 , which is independent of the depth or
371 velocity of the flow. In all cases the acceleration of the source mass following collapse was slow as it
372 flowed across the plateau at the base of the escarpment. Lateral confinement by gullies caused the flow
373 to deepen, increasing the driving stress. The flowing mass then began to accelerate rapidly, reaching a
374 maximum flow velocity exceeding that estimated from seismic records (+29%, Table 2; Pedersen *et al.*,
375 2002). As the mass flowed out from the gullies it spread and thinned, lowering the driving stress to below
376 τ_0 and causing the flow to decelerate, achieving a run-out within $\pm 1\%$ of the observed distance (best-fit: τ_0
377 = 270 kPa; Table 2). The duration of the event is best simulated with a plastic flow (+9%; Table 2), while
378 all non-plastic rheologies overestimate event duration considerably. The deposits emplaced using a
379 plastic rheology are sheet-like on all slopes and form a rounded frontal lobe with a well-defined flow front,
380 in keeping with field observations (Figure 6d). The plastic rheology therefore replicates the kinematics of
381 the event and the morphology of the resultant deposit well, with close fits obtained for the horizontal
382 displacement of the centre of mass (-28%), average and maximum deposit thickness (+6% and +18%)
383 and depositional area (+10%, Table 2).

384

385 The effect of the addition of a collisional stress coefficient (ξ) to the plastic rheology is principally to
386 reduce the velocity of the flow. With this additional velocity-dependent stress, the best-fit value of the
387 constant retarding stress obtained in the previous section must be lowered to achieve the observed run-
388 out. The maximum velocity of a flow simulated with this rheology is therefore reduced and is a closer fit to
389 that derived using seismic records (+18%; Pedersen *et al.*, 2002). In all cases the flowing mass behaved
390 in a similar manner to the previous set of simulations, and the morphology of the modelled deposits
391 shares the characteristics modelled with a purely plastic flow (Figure 6e). A number of combinations of τ_0
392 and ξ were tested, with the best-fit model simulating the event to within $\pm 0.3\%$ of the observed run-out,
393 which corresponds to: $\tau_0 = 250$ kPa, $\xi = 0.01$ (Table 2).

394

395 The kinematics of the Paatuut rock avalanche and the morphology of the resultant deposit are most
396 empirically adequate when a collisional stress coefficient ($\xi = 0.01$) is added to the plastic model ($\tau_0 = 250$

397 kPa). This rheology is most successful in reproducing the event kinematics, deposit mass distribution and
398 deposit morphology to justify the assumption that it represents, to the first order, the dominant features of
399 the emplacement dynamics. The simulated emplacement of the event is presented in Figure S2.

400

401 **4.2 Results from other simulations**

402

403 Five other rock avalanches in Vaigat were simulated using the best-fit rheological calibration obtained
404 from back analysis of the Paatuut case ($\tau_0 = 250$ kPa, $\xi = 0.01$). A realistic simulation of the observed run-
405 out was obtained for all of the rock avalanches, with all but one event modelled to within $\pm 2\%$ of the
406 observed run-out (Table 3). The model failed to adequately simulate the event characteristics of the
407 smallest event, RA 10 (ca. 5×10^6 m³), which ran out and stalled above an alluvial fan at Tupaasat
408 (Figure 5a; Table 3). A number of the deposits, particularly those emplaced by RA 1, RA 2, RA 4 and RA
409 16, are characterised by a convex upper deposit surface, and steep fronts and sides close to the angle of
410 repose. The distribution of deposit thickness, as observed through the centre line, is simulated well, with
411 those emplaced by all of the modelled events closely approximating those of the observed deposits within
412 error (Figure 7). In addition, RA 2, RA 4 and RA 10 were correctly simulated to stall at or above a major
413 topographic bench. In all cases, deposition is simulated along the full extent of the run-out path, while the
414 observed deposits were only emplaced in the medial and distal reaches. This may reflect post-deposition
415 reworking of the upper reaches of these deposits, as multiple debris flows were observed transporting
416 proximal rock avalanche sediments into the fjord. However, it may also be indicative of the simplified
417 rheology used to simulate run-out, as deposits formed using a plastic rheology remain plastic at rest,
418 even when deposited on steep slopes. Cross-slope transects taken through the toe of each deposit show
419 that the lateral thickness distribution is also simulated well, with the deposits emplaced by all of the
420 events closely approximating those of the observed deposits within error (Figure 8). The lobes of the
421 deposits appear to have developed in response to the underlying topography, with evidence of upslope
422 thinning, hole filling and pinching out of the deposit at topographic highs apparent (Figure 8).

423

424 The ability of the model to reproduce the bulk external behaviour (run-out, lateral extent, depositional

425 area, and apparent coefficient of friction H/L , which is equal to the ratio of the drop height to run-out) of
426 each of the 20 cases was assessed using reduced major axis regression (RMA; Figure 9) to compare
427 model outputs with field measurements. The total run-out distance of > 80% of the cases was simulated
428 within an error of $\pm 10\%$ using a plastic rheology and a velocity-dependent law ($\tau_0 = 250$ kPa, $\xi = 0.01$).
429 Encouragingly, half of the cases were simulated within an error of $\pm 2\%$. The RMA fit to the run-out data is
430 very close, with an r^2 value of 0.99 (Figure 9a). Residuals show spreading at relatively short run-out
431 distances (ca. 1,000 – 2,000 m) and clustering around residuals equal to 0 at long run-outs (> 3,000 m).
432 This indicates that the model simulates events that ran out over longer distances more accurately than
433 those that ran out over a shorter distance. This is perhaps unsurprising, given that the model calibration
434 was derived using the largest event of the inventory.

435

436 The energy dissipation and subsequent run-out of rock avalanches is strongly influenced by topography,
437 leading to a range of depositional surface morphologies (Okura *et al.*, 2003). The H/L of > 75% of the
438 cases was simulated within an error of $\pm 5\%$. Residuals taken from the RMA fit are well distributed,
439 although the modelled H/L for RA 3, RA 6 and RA 15 is considerably underestimated (Figure 9b). These
440 events are characterised by shorter run-out distances and planar slopes. They stall at topographic
441 benches or on an alluvial fan, having travelled over wetter, deformable substrates. Here, the model is not
442 simulating the effects of rock avalanche emplacement across different substrates. In reality, the energy
443 required to mobilise and accelerate the substrate may have been too great, causing the avalanche mass
444 to burrow into the alluvial fan or to be bulldozed into mounds (Dufresne *et al.*, 2010). In both cases, this
445 would have impeded avalanche momentum/motion and caused a decrease in mobility. Recent work has
446 also emphasised the importance of extrinsic parameters such as path materials and landslide interactions
447 with the substrate (Aaron *et al.*, 2017).

448

449 Lateral spreading at the toe of the rock avalanches is also simulated well, with the RMA regression fit to
450 the lateral extent data achieving an r^2 value of 0.91 (Figure 9c). However, the model often fails to simulate
451 the spreading of relatively short run-out rock avalanches at topographic benches and onto alluvial fans,
452 thereby considerably underestimating the lateral extent of a number of deposits (Figure 9c). Lateral

453 spreading is overestimated where, in reality, the flow has been laterally confined somewhere along its
454 run-out path (RA 11, RA 12 and RA 20). In these cases, the rock avalanches were simulated across
455 simplified terrain, which does not impose the same 3D confinement effects of topography on the rock
456 avalanche. This is also the case when considering areas of deposition, which are poorly simulated where
457 an event was emplaced across simplified terrain and for events that were partially confined, such as RA
458 19 and RA 20. These results attest to the importance of using realistic terrain models, as the dissipation
459 of mechanical energy from the rock avalanche, and thereby its mobility and spreading behaviour, is more
460 accurately simulated (Nicoletti and Sorriso-Valvo, 1991; McDougall and Hungr, 2004).

461

462 **5 Discussion**

463

464 Accurately simulating the emplacement dynamics of rock avalanches to determine parameters suited to
465 modelling beyond back-analyses is complicated. The lack of pre-, syn- and post-failure observations of
466 rock avalanches and the topography over which they travel has meant that many numerical modelling
467 studies focus on replicating the dynamics of a single (well-constrained) event. These fail to consider the
468 wider applicability and sensitivity of the rheological calibration obtained. Here, we applied a single pair of
469 rheological parameters to back-analyse the dynamics and propagation of 20 rock avalanches. The
470 general characteristics of the 20 events are simulated successfully in most cases, with the run-out of >
471 80% of the cases being simulated within an error of $\pm 10\%$. The model replicates the morphology of the
472 resultant deposits well, suggesting that approximations gained from a single back-analysis can plausibly
473 account for the observed morphology of deposits emplaced by a range of event types. The rheological
474 calibration obtained could therefore contain physically meaningful information about event emplacement
475 mechanisms that have occurred in Vaigat.

476

477 **5.1 Implications for flow behaviour**

478

479 Despite being widely used to simulate the propagation of rock avalanches (McEwan and Malin, 1989; Evans
480 *et al.*, 2001; Crosta *et al.*, 2004; Sheridan *et al.*, 2005; Pirulli, 2009; Kelfoun, 2011; Sosio *et al.*, 2012),

481 models assuming either a frictional or a Voellmy rheology failed to reproduce geometric and dynamic
482 observations at Paatuut. While the best-fit calibrations of the models used here can crudely account for the
483 observed run-out at Paatuut, the basal friction angles necessary to generate this run-out result in a long
484 duration of simulated failure with deposition concentrated in the proximal reaches of the run-out path. This
485 is at odds with the morphology of the observed deposit and the kinematic constraints of the event that were
486 estimated from seismic records. The main features of the Paatuut event can instead be reproduced using
487 a plastic rheology with a collisional stress. A number of studies have successfully simulated the run-out and
488 emplacement dynamics of volcanic debris avalanches assuming a plastic rheology (Table 4). The limited
489 ability of frictional models to simulate the run-out of the events in Vaigat may suggest that processes
490 additional to those of granular flow dynamics are important here.

491
492 The high constant retarding stresses required to correctly simulate the non-volcanic events in Vaigat and
493 Potrero de Leyes (Manzella *et al.*, 2016) may reflect: (1) differences in the intact rock strength of the
494 materials involved in these events as compared to more altered volcanic rocks, (2) differences in the
495 intrinsic physical processes operating within the flowing mass (Kelfoun *et al.*, 2009) of a rock avalanche as
496 compared to a debris avalanche, or (3) variable extrinsic substrate interactions between the settings (Aaron
497 *et al.*, 2017), including the role of water (Legros, 2002) and, in Vaigat, potential interactions with alluvium
498 and areas of permafrost. Alternatively, a high constant retarding stress may be required to realistically
499 simulate events where the failure and subsequent run-out of large volumes of material down steep slopes
500 occurred over a relatively short period of time (Takahashi and Tsujimoto, 2000; Charbonnier and Gertisser,
501 2012), as in fjords and semi-enclosed basins. The reasons for this behaviour are speculative, but are useful
502 to drive further work using a plastic rheology to simulate rock avalanches and debris avalanches in other
503 process and topographic settings, or over different substrates, to define parameter spaces for different
504 environments.

505
506 The major implication of using a plastic rheology is that flow mobility is driven by a constant stress
507 condition. This means that the friction angle at the base of these mass movements cannot be considered
508 constant. Instead, the ratio of driving to retarding stresses decreases as flow thickness increases, leading

509 to very mobile and deep flows (Charbonnier and Gertisser, 2012). Although this appears to be in keeping
510 with a number of field observations, it is difficult to explain from a mechanical perspective as it stipulates
511 that the shear stress at the base of the flow is independent of its thickness and/or its velocity (Dade and
512 Huppert, 1998). Rock avalanches exhibit complex time-dependent and spatially variable mechanical
513 behaviour, which continuum dynamic numerical models often simplify into one- or two-parameter
514 rheological laws (Iverson and Vallance, 2001). The constant stress invoked when using a plastic rheology
515 is most likely to represent an average value of a retarding stress at the flow base that varies with time
516 during rock avalanche run-out (Kelfoun, 2005). To explain this behaviour mechanically, a constant stress
517 at the base of the flow can be obtained if the basal friction angle (ϕ_{bed}) decreases with increasing flow
518 depth (h), assuming that the stress of the flow is defined by Coulomb friction (Mangeny *et al.*, 2007). For
519 example, the basal friction angle may increase more rapidly in thin flows relative to thick flows, due to the
520 presence of resistant blocks within the fluidised matrix, which act to increase the solid interaction with the
521 ground as the flow thins (Kelfoun, 2011). Alternatively, an increase of the mechanical strength of the flows
522 from their base or interior to the surface could also explain the apparent inverse relationship between flow
523 depth and friction. This strength may vary in relation to the granulometry of the flows: for example, most
524 deposits, including many of those in Vaigat, are composed of a fragmented and fluidised interior of
525 matrix-supported debris covered by a passively rafted and brittle crust of angular boulders (for example,
526 Tsergo Ri, Nepal: Heuberger *et al.*, 1984; Köfels, Austria: Brückl *et al.*, 2001; Flims, Switzerland: von
527 Poschinger *et al.*, 2006; Val Pola, Italy; Crosta *et al.*, 2007). In deeper rock avalanches, a greater
528 proportion of the flow would therefore be constituted of fine particles, prolonging flow-like capability
529 (Figure 10).

530
531 Although a plastic rheology fits the morphology of many rock avalanche deposits better than a frictional
532 rheology, the reasons for its success remain unclear at a process level. The plastic-type rheology that
533 was used here should therefore only be considered as a first order description of the rheology of the rock
534 avalanches in Vaigat. This poses fundamental questions regarding the use of simple one- or two-
535 parameter rheological laws for simulating rock avalanches. Although these laws are straightforward to
536 implement, their use is contentious as the parameters governing the rheology of the flows often lack any

537 physical meaning and remain difficult to physically quantify or validate (Schneider *et al.*, 2010; Fischer *et*
538 *al.*, 2012). In addition, the use of single-phase mass and momentum balance equations to govern flow
539 mobility only passively incorporates the effects of mechanical lubrication and fluidisation of the flow. The
540 large uncertainty associated with parameter selection for these models demands the development of
541 more sophisticated models that use physically measurable and dynamically variable values of these
542 parameters, which can actively take into account the presence of materials with different physical and
543 rheological properties and shifts between different flow regimes (Pudasaini, 2012). This property is
544 particularly important when considering the melting of snow and/or ice due to frictional heating during rock
545 avalanche propagation, which is likely to have occurred during the Paatuut event and potentially in a
546 number of other rock avalanches in Vaigat. The development of new rheological models marks the first
547 attempt to address some of these issues (Pudasaini and Krautblatter, 2014). Rather than treating the
548 effective internal and basal friction angles as constant, new models include interphase mass and
549 momentum exchanges that correspond to spatial and temporal variations in the effective solid volume
550 fraction, volume fraction of ice, friction coefficients, and lubrication/fluidisation factors that are a function
551 of a number of physical parameters or mechanical variables. The development of such models, which are
552 capable of performing dynamic strength weakening due to the effects of internal fluidisation and/or basal
553 lubrication, represents an important direction for future research, and detailed quantitative evaluation of
554 their performance with laboratory and field observations is required.

555

556 **5.2 Predictive modelling**

557

558 Physically-based simulations of rock avalanches using *VolcFlow* provide a useful tool for recognising flow
559 patterns and for calculating potential flow magnitudes, velocities, and fluxes (Crosta *et al.*, 2006). Here,
560 as in Sosio *et al.* (2008, 2012), we used a one-at-a-time (OAT) parameter calibration approach in order to
561 calibrate *VolcFlow* with data from a modern, well-constrained event. Future work will apply a multivariate
562 parameter calibration approach for multi-parameter rheologies (for example, Fischer *et al.*, 2015) in order
563 to avoid the assumption of model linearity and to capture fully the sensitivities and interactions between
564 the parameters over the full parameter space (Saltelli and Annoni, 2010). However, the model obtained

565 through OAT calibration here shows encouraging results in the model's ability to simulate a series of rock
566 avalanches using a single set of parameters obtained by back-analysis of the Paatuut event. It is
567 therefore possible that, with widely available topography and pre-failure indications that define the
568 potential volume of a failing mass, the generalised numerical modelling presented here could usefully
569 predict run-out and deposit geometry *a priori*. Such predictions would be useful in assessing future rock
570 avalanche risk and potential tsunamigenesis. The application of a model for predictive purposes, and its
571 incorporation into hazard and risk assessments, requires the development of a suitable framework, the
572 core elements of which include (i) estimation of the failure volume of the unstable rock slope in question,
573 and (ii) probabilistic run-out assessments using numerical run-out modelling.

574
575 Geometric and kinematic models of the motion of a rockslide can be identified and potential failure
576 volumes quantified using differential satellite interferometric synthetic aperture radar (InSAR), as has
577 been demonstrated in Norway (for example, Lauknes *et al.*, 2010; Blikra and Christiansen, 2014).
578 However, the use of InSAR to estimate the potential failure volume of a rock-slope requires it to be
579 actively deforming. Where this is not the case, it is possible to identify potential failure surfaces in rock-
580 slopes by their slope geometry (Jaboyedoff *et al.*, 2009). This failure surface has been termed the Sloping
581 Local Base Level (SLBL) and can be constrained by geophysical, geotechnical and/or geomorphic data
582 derived using methods such as seismic profiling and boreholes (Travelletti *et al.*, 2010). The sliding
583 surface and corresponding failure volume would then be used to constrain the source conditions of a
584 potential future event for input into numerical models of rock avalanche run-out. A caveat of this approach
585 is that the limits of stability are unlikely to be reached everywhere simultaneously and it is therefore
586 unlikely that a future failure would develop as a single event, as implied by the SLBL, and may instead
587 proceed retrogressively (Jaboyedoff *et al.*, 2009).

588
589 Although continuum dynamic models are deterministic, they can incorporate probabilistic
590 components by adopting a range of parameter values associated with different probable conditions in
591 order to compute a corresponding range in possible outcomes (Iverson, 2014). The use of non-sampling
592 methods for determining ranges of input parameter values has demonstrated particularly encouraging

593 results while preserving the simplicity and robustness of Monte Carlo-type approaches, both in simple
594 settings and when used to simulate the 1991 block-and-ash flows at Colima Volcano, Mexico (Dalbey *et*
595 *al.*, 2008). Once a prospective failure is identified, hazard maps can be constructed for risk management
596 practices by forward-modelling the event using a range of parameter values (Corominas *et al.*, 2014). Our
597 findings show that the parameter values required for scenario modelling in other settings could be
598 derived from the back-analysis of any other event provided that it occurred within similar boundary
599 conditions. However, it is important to recognise that the calibration results for the rock avalanches
600 simulated here may not be transferrable between other dynamic models, which incorporate different
601 internal stress assumptions (Hungr, 2006). It is also important to question how definitive this calibration is,
602 as particular aspects of the boundary conditions in Vaigat remain unknown (lubrication, fluidisation, basal
603 scouring, entrainment and/or deposition during motion, water absorption, ice fraction, material mixing).
604 Prior to the application of this model for predictive purposes, in-depth studies are required in order to
605 consider the effects of these conditions and the relative importance of key factors on simulated run-out.
606 Once these conditions are satisfied, a robust framework must be developed for the incorporation of the
607 model into hazard and risk assessments.

608

609 **6 Conclusions**

610

611 We have presented the results of a numerical modelling study of 20 rock avalanches in the Vaigat Strait,
612 West Greenland. Rheological calibration of the numerical flow code *VolcFlow* was performed using a well-
613 constrained event at Paatuut (AD 2000). The best-fit simulation assumes a constant retarding stress with
614 a collisional stress coefficient ($\tau_0 = 250$ kPa, $\xi = 0.01$), and simulates run-out to within $\pm 0.3\%$ of that
615 observed. Despite being widely used to simulate rock avalanche propagation, other models, that assume
616 either a frictional or a Voellmy rheology, failed to reproduce the observed event characteristics and
617 deposit distribution at Paatuut. The limited ability of frictional models to simulate the behaviour of rock
618 avalanches such as these suggests that processes additional to those of granular flow dynamics are
619 involved. Although the success of a plastic-type rheology over any other remains difficult to physically
620 explain, it might indicate that the friction angle at the base of these mass movements cannot be

621 considered constant as in many commonly used rheological models.

622

623 We applied this calibration to 19 further events, simulating rock avalanche motion across terrain of
624 varying levels of complexity. We have shown that, provided their morphological and geophysical
625 conditions are regionally consistent, a series of rock avalanches can be accurately simulated using a
626 single set of parameters obtained by back-analysis of one well-constrained event alone. *VolcFlow* can
627 plausibly account for the observed morphology of a series of deposits emplaced by events of different
628 types, although its performance is sensitive to a range of topographic and geometric factors. These
629 include: (i) the geometry of the source mass, (ii) the path topography and (iii) the substrate. The results
630 also hold important implications for our process understanding of rock avalanches in confined fjord
631 settings, where correctly modelling material flux at the point of entry into the water is critical in tsunami
632 generation. Given that mountain ranges in polar regions such as Vaigat may be candidates for sudden
633 regime shifts in rock-slope stability (Kargel *et al.*, 2013), large (tsunamigenic) rock avalanches from steep,
634 deglaciating coastlines are therefore a scenario that will need to be increasingly accommodated in risk
635 assessments in the future.

636

637 **Acknowledgments**

638

639 This work was supported by Polish National Science Centre Grant No. 2011/01/B/ST10/01553. For
640 access to *VolcFlow*, please contact Karim Kelfoun. Data for the reconstruction of DEMs at Paatuut was
641 gratefully received from Trine Dahl-Jensen at the GEUS. All other elevation data used in the modelling
642 can be obtained from the Greenland Ice Mapping Project at <https://bpcrc.osu.edu/gdg/data/gimpdem>. The
643 authors would like to thank Anja Dufresne, Martin Mergili, and two editors for providing constructive
644 reviews of this manuscript, which were gratefully received.

645

646 **References**

647

648 Aaron J, Hungr O. 2016. Dynamic simulation of the motion of partially-coherent landslides. *Engineering*

649 *Geology* **205**: 1-11.

650

651 Aaron J, McDougall S, Moore JR, Coe JA, Hungr O. 2017. The role of initial coherence and path
652 materials in the dynamics of three rock avalanche case histories. *Geoenvironmental Disasters* **4**(1): 5.

653

654 Blikra LH, Longva O, Harbitz C, Løvholt F. 2005. Quantification of rock-avalanche and tsunami hazard in
655 Storfjorden, western Norway, in Senneset K, Flaate K, Larsen JO (eds.) *Landslides and Avalanches:*
656 *Proceedings of the 11th International Conference and Field Trip on Landslides* (ICFL) Norway, 1-10
657 September 2005. London: Taylor & Francis, pp.57-64.

658

659 Blikra LH, Christiansen HH. 2014. A field-based model of permafrost-controlled rockslide deformation in
660 northern Norway. *Geomorphology* **208**: 34-49.

661

662 Böhme M, Oppikofer T, Longva O, Jaboyedoff M, Hermanns RL, Derron M-H. 2015. Analyses of past and
663 present rock slope instabilities in a fjord valley: Implications for hazard estimations. *Geomorphology* **248**:
664 464-474.

665

666 Bornhold BD, Harper JR, McLaren D, Thomson RE. 2007. Destruction of the first nations village of
667 Kwalate by a rock avalanche-generated tsunami. *Atmosphere-Ocean* **45**(2): 123-128.

668

669 Brückl E, Brückl J, Heuberger H. 2001. Present structure and prefailure topography of the giant rockslide
670 of Köfels. *Zeitschrift für Gletscherkunde und Glazialgeologie* **37**(1): 49-79.

671

672 Buchwał A, Szczuciński W, Strzelecki MC, Long AJ. 2015. New insights into the 21 November 2000
673 tsunami in West Greenland from analyses of the tree-ring structure of *Salix glauca*. *Polish Polar*
674 *Research* **36**(1): 51-65.

675

676 Charbonnier SJ, Gertisser R. 2012. Evaluation of geophysical mass flow models using the 2006 block-

677 and-ash flows of Merapi Volcano, Java, Indonesia: Towards a short-term hazard assessment tool.
678 *Journal of Volcanology and Geothermal Research* **231-232**: 87-108.

679

680 Chen H, Lee CF. 2000. Numerical simulation of debris flows. *Canadian Geotechnical Journal* **37**(1): 146-
681 160.

682

683 Chow VT. 1959. *Open-channel Hydraulics*. New York: McGraw-Hill, 680 p.

684

685 Corominas J, van Westen C, Frattini P, Cascini L, Malet J-P, Fotopoulou S, Catani F, Van Den Eeckhaut
686 M, Mavrouli O, Agliardi F, Pitilakis K, Winter MG, Pastor M, Ferlisi S, Tofani V, Hervás J, Smith JT. 2014.
687 Recommendations for the quantitative analysis of landslide risk. *Bulletin of Engineering Geology and the*
688 *Environment* **73**(2): 209-263.

689

690 Crosta GB, Chen H, Lee CF. 2004. Replay of the 1987 Val Pola landslide, Italian Alps. *Geomorphology*
691 **60**(1-2): 127-146.

692

693 Crosta GB, Imposimato S, Roddeman DG. 2006. Continuum numerical modelling of flow-like landslides,
694 in Evans SG, Mugnozza GS, Strom A, Hermanns RL (eds.) *Landslides from Massive Rock Slope Failure.*
695 *Proceedings of the NATO Advanced Research Workshop on Massive Rock Slope Failure: New Models*
696 *for Hazard Assessment*, Celano, Italy, 16-21 June 2002. Netherlands: Springer, pp.211-232.

697

698 Crosta GB, Frattini P, Fusi N. 2007. Fragmentation in the Val Pola rock avalanche. *Journal of*
699 *Geophysical Research* **112**(F1): doi:10.1029/2005JF000455.

700

701 Dade WB, Huppert HE. 1998. Long-runout rockfalls. *Geology* **26**(9): 803-806.

702

703 Dahl-Jensen T, Larsen LM, Pedersen SAS, Pedersen J, Jepsen HF, Pedersen GK, Nielsen T, Pedersen
704 AK, Platen-Hallermund FV, Weng W. 2004. Landslide and tsunami 21 November 2000 in Paatuut, West

705 Greenland. *Natural Hazards* **31**(1): 277-287.

706

707 Dalbey KR, Patra AK, Pitman EB, Bursik MI, Sheridan MF. 2008. Input uncertainty propagation methods
708 and hazard mapping of geophysical mass flows. *Journal of Geophysical Research: Solid Earth* **113**(B5):
709 16 p.

710

711 Dam G, Sønderholm M. 1998. Sedimentological evolution of a fault-controlled Early Paleocene incised
712 valley system, Nuussuaq Basin, West Greenland, in K.W Shanley, and P.J. McCabe (eds.) Relative role
713 of eustasy, climate and tectonism in continental rocks. *Society of Economic Paleontologists and*
714 *Mineralogists Special Publication*, **59**: 109-121.

715

716 Dondin F, Lebrun J-F, Kelfoun K, Fournier N, Randrianasolo A. 2012. Sector collapse at Kick'em Jenny
717 submarine volcano (Lesser Antilles): numerical simulation and landslide behaviour. *Bulletin of*
718 *Volcanology* **74**(2): 595-607.

719

720 Dufresne A, Davies TRH. 2009. Longitudinal ridges in mass movement deposits. *Geomorphology* **105**(3-
721 4): 171-181.

722

723 Dufresne A, Davies TRH, McSaveney MJ. 2010. Influence of runout-path material on emplacement of the
724 Round Top rock avalanche, New Zealand. *Earth Surface Processes and Landforms* **35**(2): 190-201.

725

726 Dufresne A, Bösmeier A, Prager C. 2016. Sedimentology of rock avalanche deposits – Case study and
727 review. *Earth-Science Reviews* **163**: 234-259.

728

729 Dufresne A, Dunning SAD. 2017. Process dependence of grain size distributions in rock avalanche
730 deposits. *Landslides* **14**(5): 1555-1563.

731

732 Dufresne A, Geertsema M, Shugar DH, Koppes M, Higman B, Haeussler PJ, Stark C, Venditti JG, Bonno

733 D, Larsen C, Gulick SP, McCall N, Walton MA, Loso M. 2018. Sedimentology and geomorphology of a
734 large tsunamigenic landslide, Taan Fiord, Alaska. *Sedimentary Geology* **364**: 302-318. .
735

736 Dykstra JL. 2013. *The post-LGM evolution of Milford Sound, Fiordland, New Zealand, timing of ice retreat,*
737 *the role of mass wasting and implications for hazards*, PhD Thesis, University of Canterbury, New
738 Zealand, 313 p.
739

740 Evans SG, Clague JJ, Woodsworth GJ, Hungr O. 1989. The Pandemonium Creek rock avalanche, British
741 Columbia. *Canadian Geotechnical Journal* **26**: 427-446.
742

743 Evans SG, Hungr O, Clague JJ. 2001. Dynamics of the 1984 rock avalanche and associated distal debris
744 flow on Mount Cayley, British Columbia, Canada; implications for landslide hazard assessment on
745 dissected volcanoes. *Engineering Geology* **61**(1): 29-51.
746

747 Evans SG, Mugnozza GS, Strom AL, Hermanns RL, Ischuk A, Vinnichenko S. 2006. Landslides from
748 massive rock slope failure and associated phenomena, in Evans SG, Mugnozza GS, Strom A, Hermanns
749 RL (eds.) *Landslides from Massive Rock Slope Failure. Proceedings of the NATO Advanced Research*
750 *Workshop on Massive Rock Slope Failure: New Models for Hazard Assessment*, Celano, Italy, 16-21
751 June 2002. Netherlands: Springer, pp.3-52.
752

753 Fischer JT, Kowalski J, Pudasaini SP. 2012. Topographic curvature effects in applied avalanche
754 modelling. *Cold Regions Science and Technology* **74-75**: 21-30.
755

756 Fischer JT, Kofler A, Fellin W, Granig M, Kleemayr K. 2015. Multivariate parameter optimization for
757 computational snow avalanche simulation. *Journal of Glaciology* **61**(229): 875-88.
758

759 Fort M, Peulvast J-P. 1995. Catastrophic mass-movements and morphogenesis in the Peri-Tibetan
760 Ranges: examples from West Kunlun, East Pamir, and Ladakh, in Slaymaker O (ed.) *Steepland*

761 *Geomorphology*. New York: John Wiley & Sons, pp.171-198.

762

763 Gauthier D, Anderson SA, Fritz HM, Giachetti T. 2017. Karrat Fjord (Greenland) tsunamigenic landslide of
764 17 June 2017: initial 3D observations. *Landslides* 1-6, doi:10.1007/s10346-017-0926-4.

765

766 Giachetti T, Paris R, Kelfoun K, Perez-Torrado FJ. 2011. Numerical modelling of the tsunami triggered by
767 the Güimar debris avalanche, Tenerife (Canary Islands): Comparison with field-based data. *Marine*
768 *Geology* **284**(1-4): 189-202.

769

770 Giachetti T, Paris R, Kelfoun K, Ontowirjo B. 2012. Tsunami hazard related to a flank collapse of Anak
771 Krakatau Volcano, Sunda Strait, Indonesia. *Geological Society, London, Special Publications* **361**(1): 79-
772 90.

773

774 Gigli G, Fanti R, Canuti P, Casagli N. 2011. Integration of advanced monitoring and numerical modelling
775 techniques for the complete risk scenario analysis of rockslides: The case of Mt. Beni (Florence, Italy).
776 *Engineering Geology* **120**(1-4): 48-59.

777

778 Harbitz CB, Glimsdal S, Løvholt F, Kveldevik V, Pedersen GK, Jensen A 2014. Rockslide tsunamis in
779 complex fjords: From an unstable rock slope at Åkerneset to tsunami risk in western Norway. *Coastal*
780 *Engineering* **88**: 101-122.

781

782 Heuberger H, Masch L, Preuss E, Strecker A. 1984. Quaternary landslides and rock fusion in Central
783 Nepal and the Tyrolean Alps. *Mountain Research and Development* **4**(4): 345-362.

784

785 Hovius N, Stark C, Allen P. 1997. Sediment flux from a mountain belt derived by landslide mapping.
786 *Geology* **25**(3): 231-234.

787

788 Howat IM, Negrete A, Smith BE. 2014. The Greenland Ice Mapping Project (GIMP) land classification and

789 surface elevation datasets. *The Cryosphere* **8**(4): 1509-1518.

790

791 Huggel C, Zraggen-Oswald S, Haeberli W, Käab A, Polkvoj A, Galushkin I, Evans SG. 2005. The 2002
792 rock/ice avalanche at Kolka/Karmadon, Russian Caucasus: assessment of extraordinary avalanche
793 formation and mobility, and application of QuickBird satellite imagery. *Natural Hazards and Earth System
794 Sciences* **5**(2): 173-187.

795

796 Humlum O. 2000. The geomorphic significance of rock glaciers: estimates of rock glacier debris volumes
797 and headwall recession rates in West Greenland. *Geomorphology* **35**(1-2): 41-67.

798

799 Hungr O. 1995. A model for the runout analysis of rapid flow slides, debris flows, and avalanches. *Canadian
800 Geotechnical Journal* **32**(4): 610-623.

801

802 Hungr O, Evans SG. 2004. Entrainment of debris in rock avalanches; an analysis of a long run-out
803 mechanism. *Geological Society of America Bulletin* **116**(9/10): 1240-1252.

804

805 Hungr O. 2006. Rock avalanche occurrence, process and modelling, in Evans SG, Mugnozza, GS, Strom
806 A, Hermanns RL (eds.) *Landslides from Massive Rock Slope Failure. Proceedings of the NATO
807 Advanced Research Workshop on Massive Rock Slope Failure: New Models for Hazard Assessment,*
808 Celano, Italy, 16-21 June 2002. Netherlands: Springer, pp.243-266.

809

810 Hutter K, Nohguchi U. 1990. Similarity solutions for a Voellmy model of snow avalanches with finite mass.
811 *Acta Mechanica* **82**(1-2): 99-127.

812

813 Iverson RM, Reid M, Lahusen R. 1997. Debris flow mobilization from landslides. *Annual Reviews Earth
814 Planetary Sciences* **25**: 85-138.

815

816 Iverson RM, Vallance JW. 2001. New views of granular mass flows. *Geology* **29**(2): 115-118.

817

818 Iverson RM. 2014. Debris flows: behaviour and hazard assessment. *Geology Today* **30**(1): 15-20.

819

820 Jaboyedoff M, Couture R, Locat P. 2009. Structural analysis of Turtle Mountain (Alberta) using digital
821 elevation model: Toward a progressive failure. *Geomorphology* **103**(1): 5-16.

822

823 Jaboyedoff M, Oppikofer T, Derron M-H, Blikra LH, Böhme M, Saintot A. 2011. Complex landslide behaviour
824 and structural control: a three-dimensional conceptual model of Åknes rockslide, Norway. *Geological
825 Society, London, Special Publications* **351**: 147-161.

826

827 Kargel J, Bush A, Leonard G. 2013. Arctic warming and sea ice diminution herald
828 changing glacier and cryospheric hazard regimes. European Geophysical Union, General Assembly
829 Conference Abstracts **15**:14188.

830

831 Kelfoun K, Druitt TH. 2005. Numerical modelling of the emplacement of Socompa rock avalanche, Chile.
832 *Journal of Geophysical Research* **110**(B12), doi:10.1029/2005JB003758.

833

834 Kelfoun K, Druitt TH, de Vries BVW, Guilbaud M-N. 2008. Topographic reflection of the Socompa debris
835 avalanche, Chile. *Bulletin of Volcanology* **70**(10): 1169-1187.

836

837 Kelfoun K, Samaniego P, Palacios P, Barba D. 2009. Testing the suitability of frictional behaviour for
838 pyroclastic flow simulation by comparison with a well-constrained eruption at Tungurahua volcano
839 (Ecuador). *Bulletin of Volcanology* **71**(9): 1057-1075.

840

841 Kelfoun K, Giachetti T, Labazuy P. 2010. Landslide-generated tsunamis at Reunion Island. *Journal of
842 Geophysical Research* **115**(F4), doi:10.1029/2009JF001381.

843

844 Kelfoun K. 2011. Suitability of simple rheological laws for the numerical simulation of dense pyroclastic

845 flows and long-runout volcanic avalanches. *Journal of Geophysical Research* **116**(B8),
846 doi:10.1029/2010JB007622.

847

848 Kelfoun K. 2017. A two-layer depth-averaged model for both the dilute and the concentrated parts of
849 pyroclastic currents. *Journal of Geophysical Research Solid Earth* **122**: 4293-4311,
850 doi:10.1002/2017JB014013.

851

852 Kelfoun K, Gueugneau V, Komorowski J-C, Aisyah N, Cholik N, Merciecca C. 2017. Simulation of block-
853 and-ash flows and ash-cloud surges of the 2010 eruption of Merapi volcano with a two-layer
854 model. *Journal of Geophysical Research Solid Earth* **122**: 4277-4292, doi:10.1002/2017JB013981.

855

856 Korup O. 2002. Recent research on landslide dams - a literature review with special attention to New
857 Zealand. *Progress in Physical Geography* **26**(2): 206-235.

858

859 Korup O. 2006. Effects of large deep-seated landslides on hillslope morphology, western Southern Alps,
860 New Zealand. *Journal of Geophysical Research: Earth Surface* **111**(F1), 18 p.

861

862 Korup O, Clague JJ, Hermanns RL, Hewitt K, Strom AL, Weidinger JT. 2007. Giant landslides,
863 topography and erosion. *Earth and Planetary Science Letters* **261**(3-4): 578-589.

864

865 Larsen IJ, Montgomery DR, Korup O. 2010. Landslide erosion controlled by hillslope material. *Nature*
866 *Geoscience* **3**(4): 247-251.

867

868 Lauknes TR, Piyush Shanker A, Dehls JF, Zebker HA, Henderson IHC, Larsen Y. 2010. Detailed
869 rockslide mapping in northern Norway with small baseline and persistent scatterer interferometric SAR
870 time series methods. *Remote Sensing of Environment* **114**(9): 2097-2109.

871

872 Long AJ, Woodroffe SA, Roberts DH, Dawson S. 2011. Isolation basins, sea-level changes and the

873 Holocene history of the Greenland Ice Sheet. *Quaternary Science Reviews* **30**: 3748-3768.
874

875 Louge MY. 2003. A model for dense granular flows down bumpy inclines, *Physical Review E* **76**(6): 11 p.
876

877 Løvholt F, Pedersen G, Harbitz CB, Glimsdal S, Kim J. 2015. On the characteristics of landslide tsunamis.
878 *Philosophical Transactions of the Royal Society of London A* **373**(2053): 18.
879

880 Luna BQ, van Westen CJ, Jetten V, Cepeda J, Stumpf A, Malet J-P, van Asch TWJ. 2010. A preliminary
881 compilation of calibrated rheological parameters used in dynamic simulations of landslide run-out, in Malet
882 J-P, Glade T, Casagli N. (eds.) *Mountain risks: bringing science to society. Proceedings of the Mountain
883 Risks International Conference*. Firenze, Italy: CERG Strasbourg, pp.255-260.
884

885 Malamud BD, Turcotte DL, Guzzetti F, Reichenbach P. 2004. Landslide inventories and their statistical
886 properties. *Earth Surface Processes and Landforms* **29**(6): 687-711.
887

888 Mangeney A, Bouchut F, Thomas N, Vilotte J-P, Bristeau MO. 2007. Numerical modelling of self-
889 channeling granular flows and of their levee-channel deposits. *Journal of Geophysical Research* **112**(F2),
890 doi:10.1029/2006JF000469.
891

892 Manzella I, Penna I, Kelfoun K, Jaboyedoff M. 2016. High-mobility of unconstrained rock avalanches:
893 Numerical simulations of a laboratory experiment and an Argentinian event, in S. Aversa, L. Cascini, L.
894 Picarelli, and C. Scavia (eds.) *Landslides and Engineered Slopes: Experience, Theory, Practice*. Rome:
895 Balkema, pp.1345-1352.
896

897 McDougall S, Hungr O. 2004. A model for the analysis of rapid landslide motion across three-dimensional
898 terrain. *Canadian Geotechnical Journal* **41**(6): 1084-1097.
899

900 McDougall S. 2006. *A new continuum dynamic model for the analysis of extremely rapid landslide motion*

901 *across complex 3D terrain*, PhD Thesis, University of British Columbia, Canada, 268 p.
902

903 Mergili M, Fischer J-T, Krenn J, Pudasaini SP. 2017. r.avaflow v1, an advanced open-source
904 computational framework for the propagation and interaction of two-phase mass flows. *Geoscientific*
905 *Model Development* **10**(2): 553-569.
906

907 Miller DJ. 1960. The Alaska earthquake of July 10, 1958: giant wave in Lituya Bay. *Bulletin of the*
908 *Seismological Society of America* **50**(2): 253-266.
909

910 Moore JR, Pankow KL, Ford SR, Koper KD, Hale JM, Aaron J, Larsen CF. 2017. Dynamics of the
911 Bingham Canyon rock avalanches (Utah, USA) resolved from topographic, seismic, and infrasound data.
912 *Journal of Geophysical Research* **122**(3): 615-640, doi:10.1002/2016JF004036.
913

914 Murty TS. 1979. Submarine slide-generated water waves in Kitimat, British Columbia. *Journal of*
915 *Geophysical Research* **84**(C12), doi:10.1029/JC084iC12p07777.
916

917 Nicoletti PG, Sorriso-Valvo M. 1991. Geomorphic controls of the shape and mobility of rock avalanches.
918 *Geological Society of America Bulletin* **103**(10): 1365-1373.
919

920 Noh MJ, Howat IM. 2015. Automated stereo-photogrammetric DEM generation at high latitudes: Surface
921 Extraction with TIN-based Search-space Minimization (SETSM) validation and demonstration over
922 glaciated regions. *GIScience and Remote Sensing* **52**(2): 198-217.
923

924 Okura YH, Kitahara H, Kawanami A, Kurokawa U. 2003. Topography and volume effects on travel
925 distance of surface failure. *Engineering Geology* **67**(3-4): 243-254.
926

927 Olesen O, Blikra LH, Braathen A, Dehls JF, Olsen L, Rise L, Roberts D, Riis F, Faleide JI, Anda E. 2004.
928 Neotectonic deformation in Norway and its implications: a review. *Norwegian Journal of Geology* **84**: 3-

929 34.
930
931 Oreskes N, Shrader-Frechette K, Belitz K. 1994. Verification, validation, and confirmation of numerical
932 models in the earth sciences. *Science* **263**(5147): 641-646.
933
934 Paris R, Giachetti T, Chevalier J, Guillou H, Frank N. 2011. Tsunami deposits in Santiago Island (Cape
935 Verde archipelago) as possible evidence of a massive flank failure of Fogos volcano. *Sedimentary
936 Geology* **239**(3-4): 129-145.
937
938 Paris R, Bravo JJC, González MEM, Kelfoun K, Nauret F. 2017. Explosive eruption, flank collapse and
939 megatsunami at Tenerife ca. 170 ka. *Nature Communications* **8**: 15246.
940
941 Pedersen GK, Pulvertaft TCR. 1992. The nonmarine Cretaceous of the West Greenland basin, onshore
942 West Greenland. *Cretaceous Research* **13**: 263-272.
943
944 Pedersen SAS, Foged N, Frederiksen J. 1989. Extent and economic significance of landslides in
945 Denmark, Faroe Islands and Greenland, in Brabb EE, Harrod BL (eds.) *Landslides, extent and economic
946 significance*. Rotterdam: Balkema, pp.153-156.
947
948 Pedersen SAS, Larsen LM, Dahl-Jensen T, Jepsen HF, Pedersen GK, Nielsen T, Pedersen AK, Platen-
949 Hallermund FV, Weng W. 2002. Tsunami-generating rock fall and landslide on the south coast of
950 Nuussuaq, central West Greenland. *Geological Survey of Denmark and Greenland Bulletin* **191**: 73-83.
951
952 Pirulli M, Mangeney A. 2008. Results of back-analysis of the propagation of rock avalanches as a function
953 of the assumed rheology. *Rock Mechanics and Rock Engineering* **41**(1): 59-84.
954
955 Pirulli M. 2009. The Thurwieser rock avalanche (Italian Alps): Description and dynamic analysis.
956 *Engineering Geology* **109**: 80-92.

957

958 Poli P. 2017. Creep and slip: Seismic precursors to the Nuugaatsiaq landslide (Greenland). *Geophysical*
959 *Research Letters* **44**(17): 8832-8836.

960

961 Pudasaini SP. 2012. A general two-phase debris flow model. *Journal of Geophysical Research* **117**(F3),
962 doi:10.1029/2011JF002186.

963

964 Pudasaini SP, Krautblatter M. 2014. A two-phase mechanical model for rock-ice avalanches. *Journal of*
965 *Geophysical Research* **119**(10), doi:10.1002/2014JF003183.

966

967 Rickenmann D. 2005. Runout prediction methods, in Jakob M, Hungr O (eds.) *Debris-flow hazards and*
968 *related phenomena*. Berlin: Springer, pp.305-324.

969

970 Saltelli A, Annoni P. 2010. How to avoid a perfunctory sensitivity analysis. *Environmental Modelling &*
971 *Software* **25**(12): 1508-17.

972

973 Savage SB, Hutter K. 1989. The motion of a finite mass of granular material down a rough incline. *Journal*
974 *of Fluid Mechanics* **199**: 177-215.

975

976 Schneider D, Bartelt P, Caplan-Auerbach J, Christen M, Huggel C, McArdell BW. 2010. Insights into rock-
977 ice avalanche dynamics by combined analysis of seismic recordings and a numerical avalanche model.
978 *Journal of Geophysical Research* **115**(F4), doi:10.1029/2010JF001734.

979

980 Schleier M, Hermanns RL, Gosse JC, Oppikofer T, Rohn J, Tønnesen JF. 2017. Subaqueous rock-
981 avalanche deposits exposed by post-glacial isostatic rebound, Innfjordalen, Western Norway.
982 *Geomorphology* **289**: 117-133.

983

984 Sepúlveda S, Serey A. 2009. Tsunamigenic, earthquake-triggered rock slope failures during the April 21,

985 2007 Aisén earthquake, southern Chile (45.5°S). *Andean Geology* **36**(1): 131-136.

986

987 Sheridan MF, Stinton AJ, Patra A, Pitman EB, Bauer A, Nichita CC. 2005. Evaluating Titan 2D mass-flow
988 model using the 1963 Little Tahoma Peak avalanches, Mount Rainier, Washington. *Journal of*
989 *Volcanology and Geothermal Research* **139**: 89-102.

990

991 Sosio R, Crosta GB, Hungr O. 2008. Complete dynamic modelling calibration for the Thurwieser rock
992 avalanche (Italian Central Alps). *Engineering Geology* **100**(1): 11-26.

993

994 Sosio, R, Crosta GB, Chen JH, Hungr O. 2012. Modelling rock avalanche propagation onto glaciers.
995 *Quaternary Science Reviews* **47**: 23-40.

996

997 Strom AL. 2004. Rock avalanches of the Ardon River valley at the southern foot of the Rocky Range,
998 Northern Caucasus, North Osetia. *Landslides* **1**(3): 237-241.

999

1000 Szczuciński W, Rosser NJ, Strzelecki MC, Long AJ, Lawrence T, Buchwal A, Chagué-Goff C, Woodroffe
1001 S. 2012. Sedimentary Record and Morphological Effects of a Landslide-Generated Tsunami in a Polar
1002 Region: The 2000 AD Tsunami in Vaigat Strait, West Greenland, American Geophysical Union, Fall
1003 Meeting 2012, Abstract #OS33B-1820.

1004

1005 Takahashi T, Tsujimoto H. 2000. A mechanical model for Merapi-type pyroclastic flow. *Journal of*
1006 *Volcanology and Geothermal Research* **98**(1-4): 91-115.

1007

1008 Travelletti J, Demand J, Jaboyedoff M, Marillier F. 2010. Mass movement characterization using a
1009 reflexion and refraction seismic survey with the sloping local base level concept. *Geomorphology* **116**(1):
1010 1-10.

1011

1012 Voight B, Faust C. 1982. Frictional heat and strength loss in some rapid landslides. *Géotechnique* **32**(1):

1013 43-54.

1014

1015 Voight B, Janda RJ, Glicken H, Douglass PM. 1983. Nature and mechanics of the Mount St. Helens
1016 rockslide-avalanche of 18 May 1980. *Géotechnique* **33**(3): 243-273.

1017

1018 von Poschinger A, Wassmer P, Maisch M. 2006. The Flims rockslide: History of interpretation and new
1019 insights, in Evans SG, Mugnozsa GS, Strom A, Hermanns RL (eds.) *Landslides from Massive Rock Slope*
1020 *Failure. Proceedings of the NATO Advanced Research Workshop on Massive Rock Slope Failure: New*
1021 *Models for Hazard Assessment*, Celano, Italy, 16-21 June 2002. Netherlands: Springer, pp.329-356.

1022

1023 Voss P, Poulsen SK, Simonsen SB, Gregersen S. 2007. Seismic hazard assessment of Greenland.
1024 *Geological Survey of Denmark and Greenland Bulletin* **13**: 57-60.

1025

1026 Wadge G, Jackson P, Bower SM, Woods AW, Calder E. 1998. Computer simulations of pyroclastic flows
1027 from dome collapse. *Geophysical Research Letters* **25**(19): 3677-3680, doi:10.1029/98GL0071.

1028

1029 Willenberg H, Eberhardt E, Loew S, McDougall S, Hungr O. 2009. Hazard assessment and runout analysis
1030 for an unstable rock slope above an industrial site in the Riviera valley, Switzerland. *Landslides* **6**(2): 111-
1031 116.

1032

1033 Willgoose G, Hancock G. 1998. Revisiting the hypsometric curve as an indicator of form and process in
1034 transport-limited catchments. *Earth Surface Processes and Landforms* **23**(7): 611-623.

Tables

Table 1. Characteristics of the Paatuut rock avalanche (RA 1).

	Observation
Maximum run-out (m)*	4,383
Lateral extent at toe (m)*	1,325
Maximum flow velocity (m s ⁻¹)†	56
Average flow velocity (m s ⁻¹)†	37
Duration of emplacement (s)†	80
Maximum deposit thickness (m)*	60
Depositional area (m ²)*	4,138,971
Hypsometric integral (-)*	0.235
Centre of mass displacement, horizontal (m)*	2,353

* Description provided in Text S1 (Supporting Information).

† From Pedersen *et al.* (2002) and Dahl-Jensen *et al.* (2004).

Table 2. Parameters and results of the best-fit simulation of the Paatuut rock avalanche (RA 1), for each rheology. Percentage variations relative to field data are provided in brackets.

	<i>Rheology</i>				
	Frictional (1 angle)	Frictional (2 angles)	Voellmy	Plastic	Plastic + C
<i>Mechanical behaviour</i>					
Density (kg m ⁻³)	2,150	2,150	2,150	2,150	2,150
Basal friction angle, φ_{bed} (°)	14	12	13	-	-
Internal friction angle, φ_{int} (°)	-	30	-	-	-
Collisional stress coefficient, ξ (-)	-	-	0.01	-	0.01
Cohesion, τ_0 (kPa)	-	-	-	270	250
<i>Model predictions</i>					
Max. run-out (m)	4,503 (+3%)	4,319 (-2%)	4,134 (-6%)	4,334 (-1%)	4,368 (-0.3%)
Max. flow velocity (m s ⁻¹)	89 (+59%)	100 (+79%)	48 (-14%)	72 (+29%)	66 (+18%)
Duration of emplacement (s)	184 (+130%)	249 (+211%)	243 (+204%)	87 (+9%)	92 (+15%)
Max. deposit thickness (m)	106 (+77%)	111 (+85%)	110 (+83%)	71 (+18%)	72 (+20%)
Lateral extent at toe (m)	1,353 (+2%)	984 (-39%)	1,546 (+17%)	821 (-38%)	1,101 (-17%)
Depositional area (m ²)	5,579,375 (+35%)	4,155,625 (+0.4%)	4,898,750 (+18%)	4,563,125 (+10%)	4,545,000 (+10%)
Hypsometric integral (-)	0.138 (-41%)	0.100 (-57%)	0.150 (-36%)	0.272 (+16%)	0.269 (+14%)
X-displacement of the centre of mass (m)	1,617 (-31%)	308 (-87%)	1,885 (-20%)	1,694 (-28%)	1,776 (-25%)
Average flow velocity (m s ⁻¹)	25 (-32%)	29 (-22%)	7 (-81%)	20 (-45%)	29 (-21%)
Average deposit thickness (m)	15 (-17%)	11 (-39%)	16 (-11%)	19 (+6%)	19 (+6%)
			<25%	25-50%	>50%

Table 3. Results of the simulations of five rock avalanches simulated using parameters obtained in *Section 4.1*. Percentage variations relative to field data are provided in brackets, where available.

	<i>Event</i>				
	RA 2	RA 4	RA 10	RA 14	RA 16
<i>Model predictions</i>					
Max. run-out (m)	2,060 (-1%)	2,829 (-0.5%)	1,643 (-9%)	3,123 (-2%)	2,299 (-2%)
Max. flow velocity (m s ⁻¹)	61 -	83 -	36 -	64 -	59 -
Duration of emplacement (s)	52 -	50 -	59 -	61 -	54 -
Max. deposit thickness (m)	22 (-8%)	25 (-28%)	72 (+41%)	34 (-19%)	27 (+12%)
Lateral extent at toe (m)	241 (-23%)	702 (+8%)	716 (-3%)	889 (-4%)	1,055 (+3%)
Depositional area (m ²)	1,120,625 (+12%)	2,233,125 (+16%)	804,375 (+33%)	2,294,375 (+9%)	1,773,125 (+26%)
Hypsometric integral (-)	0.447 (+7%)	0.389 (+8%)	0.239 (-39%)	0.361 (+11%)	0.348 (+3%)
X-displacement of the centre of mass (m)	843 (-12%)	1,373 (-11%)	667 (-24%)	1,448 (-2%)	1,302 (-7%)
Average flow velocity (m s ⁻¹)	24 -	33 -	9 -	27 -	24 -
Average deposit thickness (m)	10 (0%)	10 (-17%)	18 (-10%)	13 (-7%)	9 (-11%)
			< 25%	25 – 50%	> 50%

Table 4. Examples of long run-out events successfully modelled using a plastic rheology (*VolcFlow*).

<i>Event</i>	<i>Type</i>	<i>Volume (× 10⁶ m³)</i>	<i>Run-out (km)</i>	<i>τ₀, ξ (kPa, -)</i>	<i>Reference</i>
Vaigat (<i>n</i> = 20)	Rock avalanche	2 – 90	1.2 – 4.4	250, 0.01	This study
Fogo	Debris avalanche, tsunami	115,000	40	90 – 95*	Paris <i>et al.</i> (2011)
Güïmar	Debris avalanche, tsunami	44,000	38	145 – 150*	Giachetti <i>et al.</i> (2011)
Socompa	Debris avalanche	36,000	40	52	Kelfoun and Druitt (2005)
Las Cañadas	Debris avalanche, tsunami	12,000	46	50	Paris <i>et al.</i> (2017)
Réunion Island	Debris avalanche, tsunami	10,000	35 – 40	20 – 50*	Kelfoun <i>et al.</i> (2010)
Potrero de Leyes	Rock avalanche	250	5.1	200	Manzella <i>et al.</i> (2016)

*Exact value of τ_0 dependent upon whether single or retrogressive failure of the rock mass is defined, as well as the value of the stress exerted by the water as defined in *VolcFlow*.

Figures

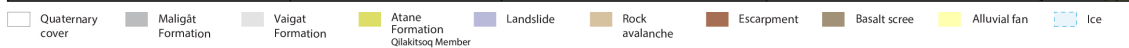
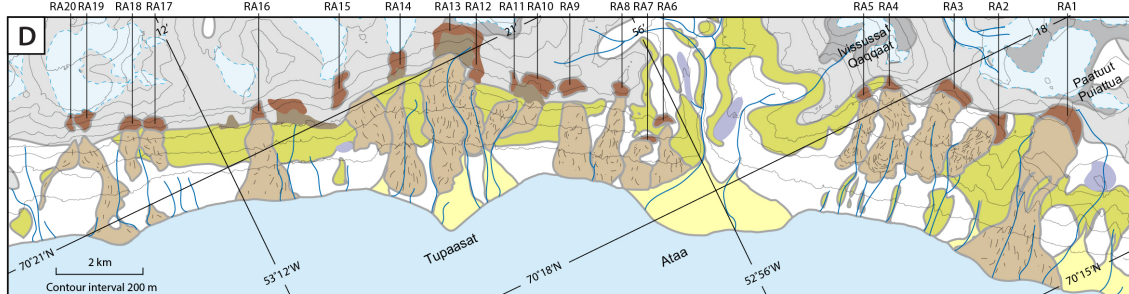
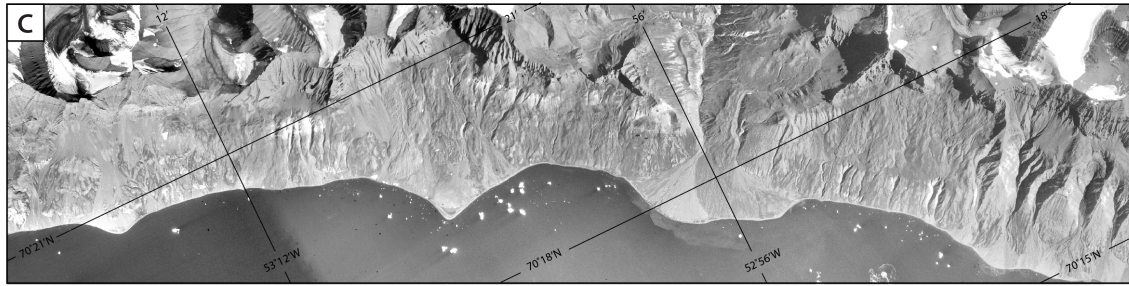
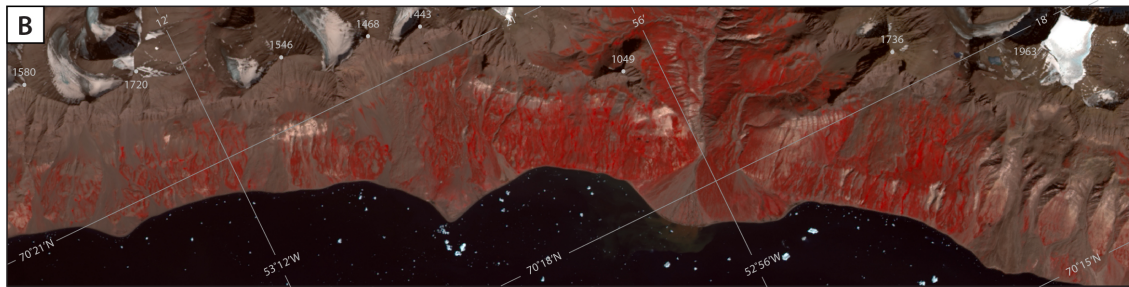
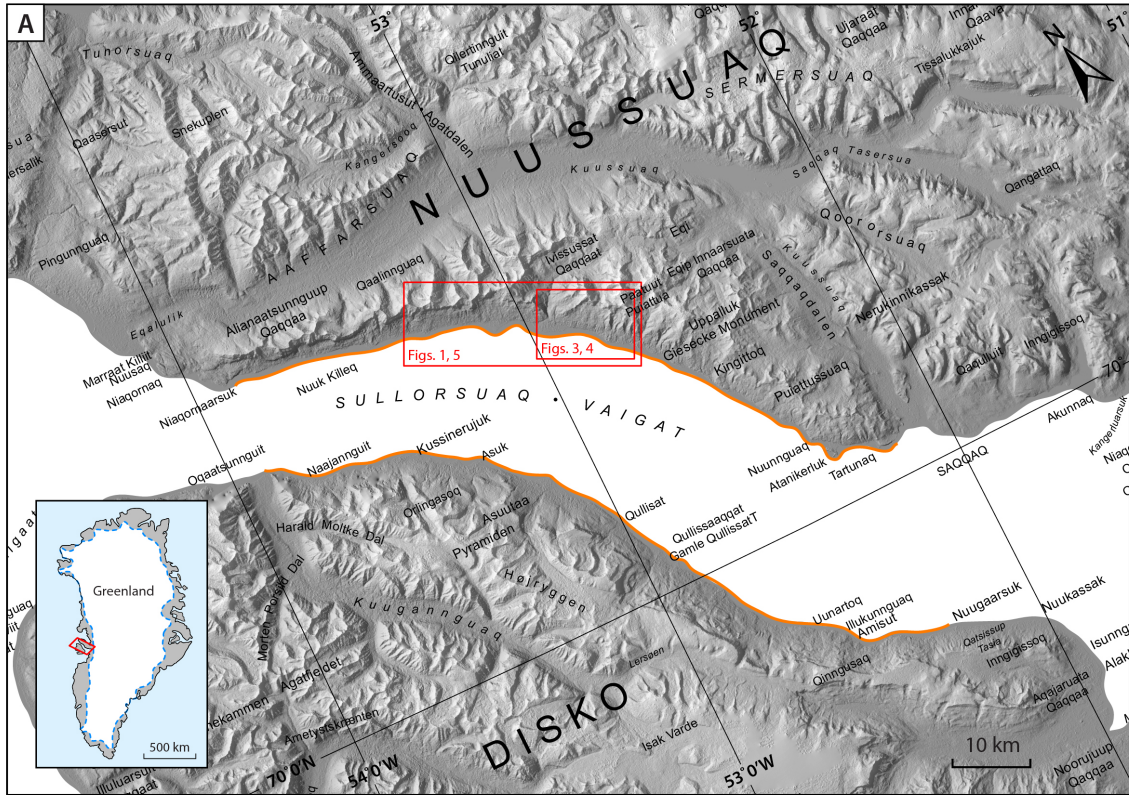


Figure 1. (a) Map of the Vaigat Strait (Sullorsuaq) with coastlines prone to rock slope failure indicated in orange (for location within Greenland, see inset). Frames and figure numbers indicate coverage of detailed maps. Digital elevation data from the Greenland Mapping Project (Howat *et al.*, 2014), (b) Pan-sharpened false color Landsat-8 image of the area, acquired on 22/07/2016 (15 m), (c) Vertical aerial photographs of the south coast of Nuussuaq, West Greenland, taken in 1985 (5 m), and (d) Geological map of area, showing 20 large rock avalanche deposits. Names are given in (d) and used throughout. Contours are drawn in 200 m intervals from the 25 m Greenland Mapping Project DEM (Howat *et al.*, 2014). The geometric characteristics of the rock avalanches are summarised in Table S1 (Supporting Information).

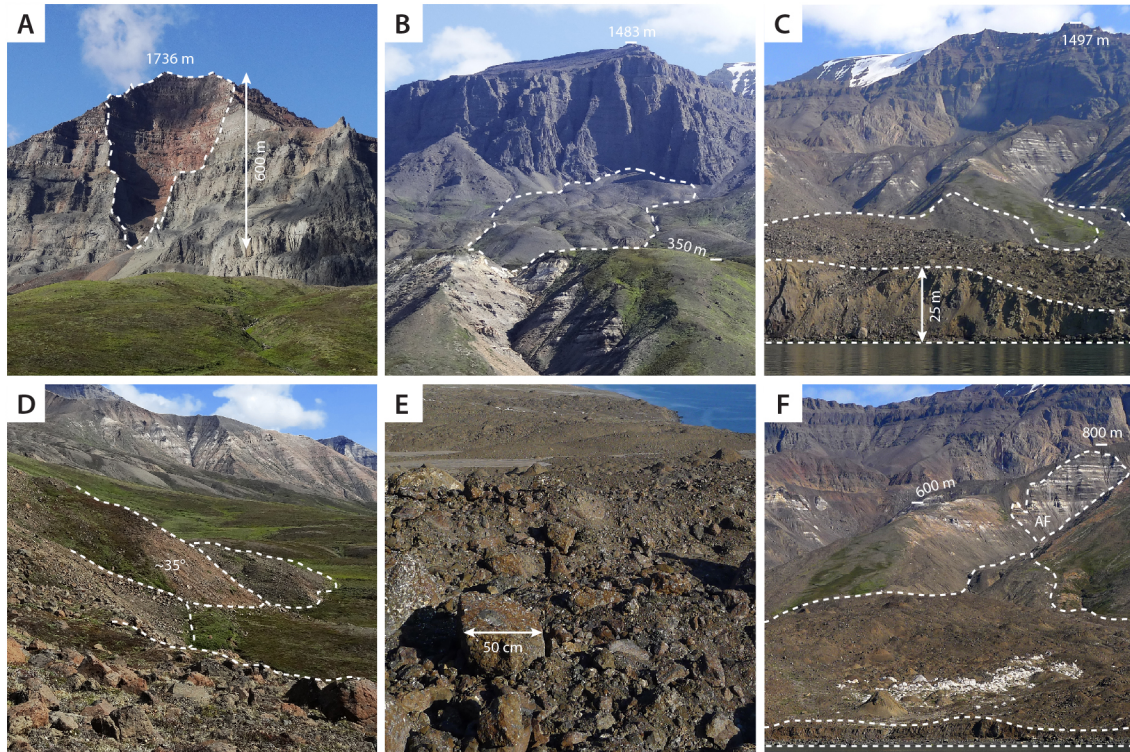


Figure 2. (a) Source area of RA 4, characterised by fresh surfaces and burnt lithologies, (b) View onto RA 2 deposits, which stalled on a topographic bench, (c) View from ca. 100 m offshore looking onto the rock avalanche toe deposit at Paatuut (RA 1), (d) Steep, lobate deposits emplaced by RA 4, (e) View onto the surface of the deposit at Paatuut, which is characterised by coarse material, and (f) View from offshore looking onto the deposit at Paatuut, which is characterised by a field of conical mounds.

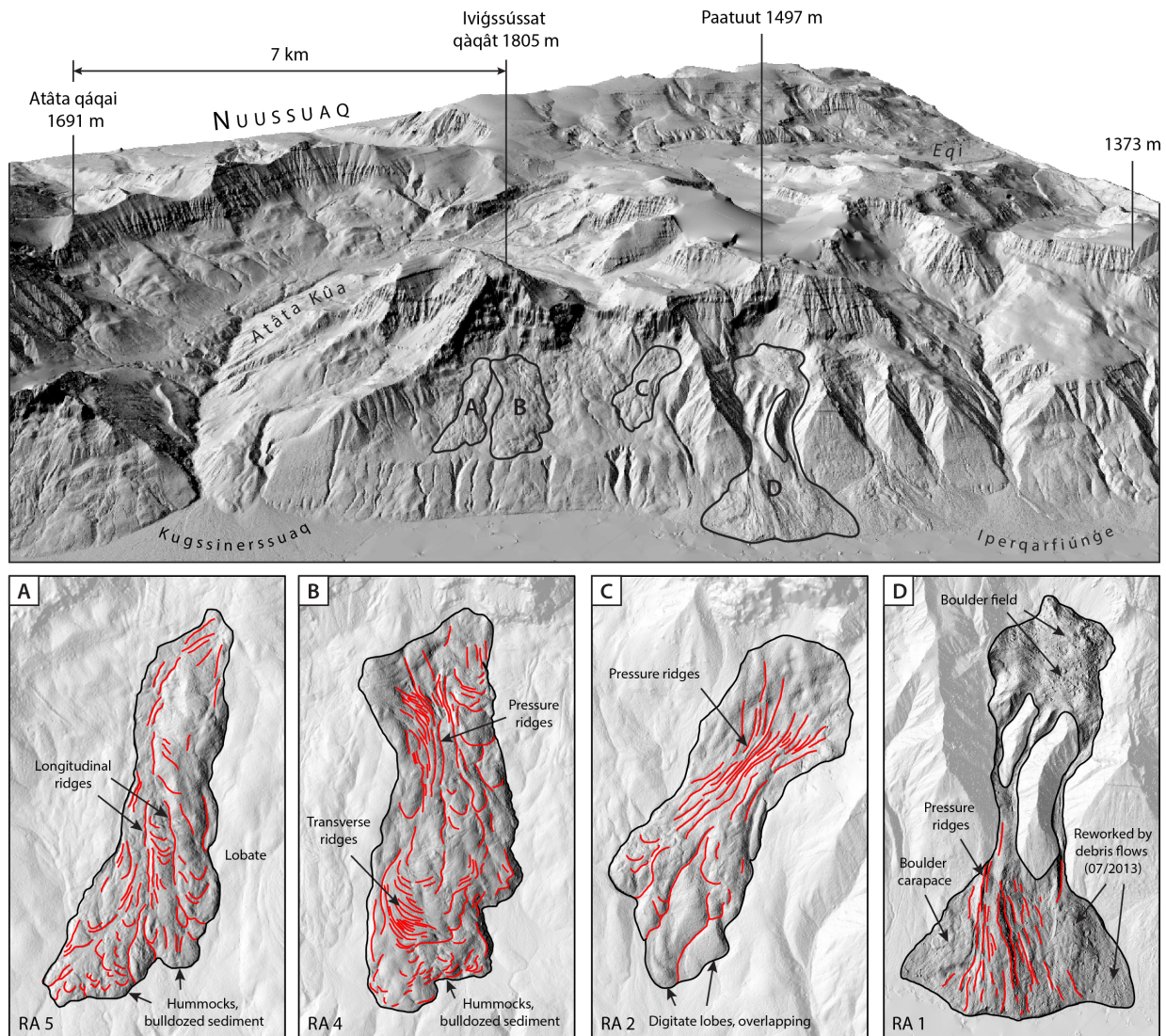


Figure 3. A 3D perspective view of rock avalanche deposits in Vaigat, West Greenland, looking north from a position above the Vaigat Strait. The surface morphology of four rock avalanches, labelled a – d, is mapped and annotated below. 0.5 m satellite imagery was acquired on 19 June 2012 by WorldView-1 and orthorectified to produce a 2 m DEM (Noh and Howat, 2015).

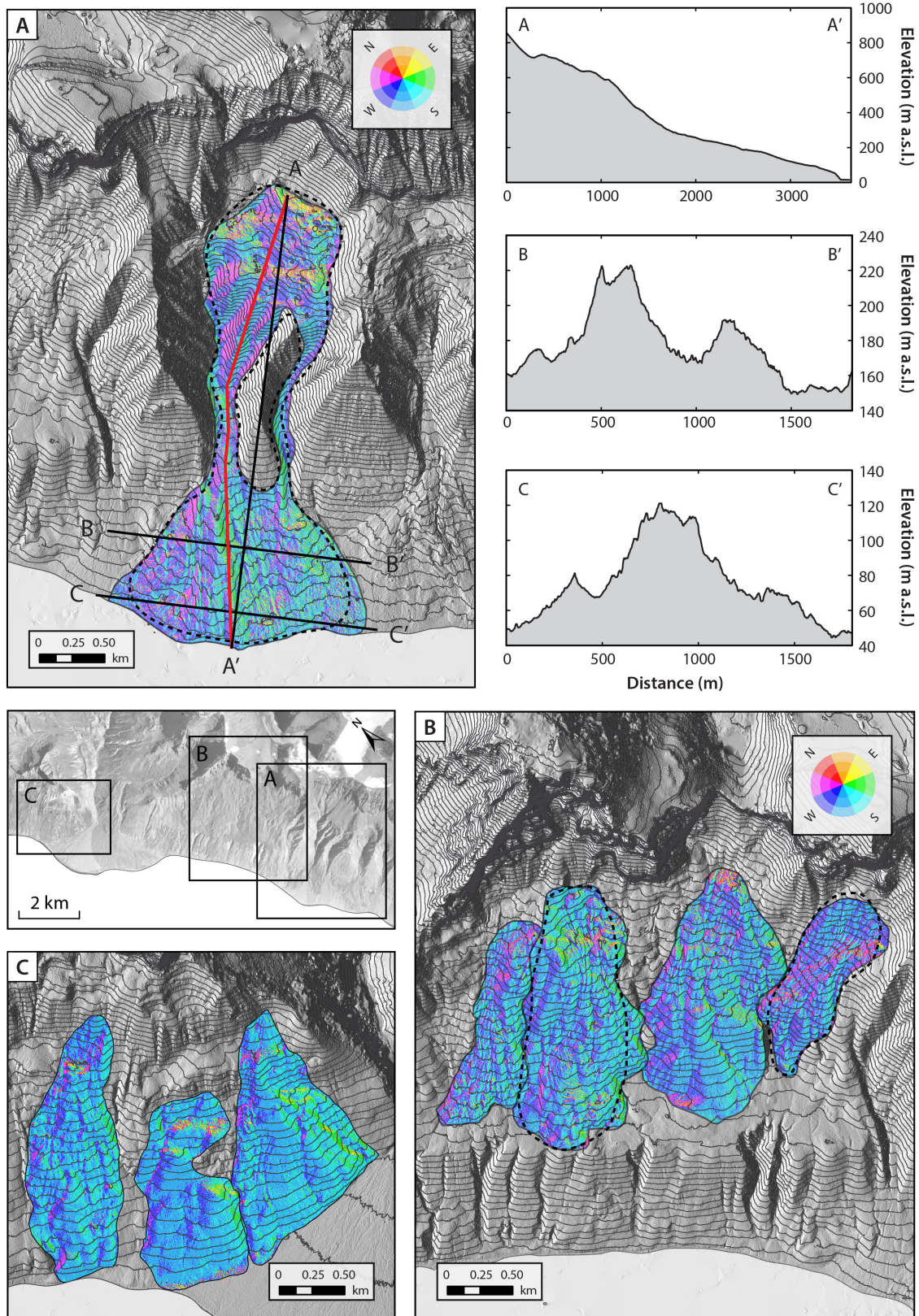


Figure 4. Slope-aspect maps showing the surface morphology of (a) the Paatuut rock avalanche deposit (RA 1), (b) RA 2 – 5, and (c) RA 6 – 8. Topographic contour interval is 20 m. The Paatuut slide passed through two steep gullies before being deposited on slopes with a dip of $6 - 9^\circ$ (A – A'). The lower part of the slide comprises two lobes (represented by the cross-profile B – B') that merge downwards into one (C – C'). The best-fit modelling results are superposed on the post-event topography (black dashed lines). Red line A – A' represents transects used for modelling comparisons in Figure 6. Elevation data from Noh and Howat (2015).

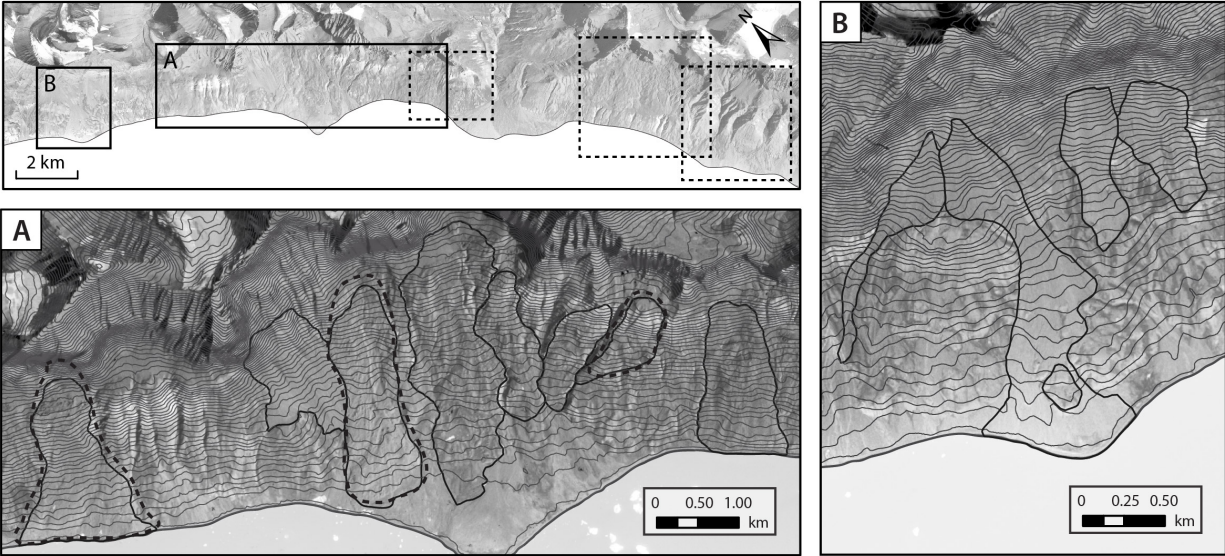


Figure 5. Rock avalanche deposits in Vaigat, West Greenland. (a) Aerial photo showing the surface morphology of RA 9 – 16, (b) aerial photo showing the surface morphology of RA 17 – 20. Topographic contour interval is 20 m. The best-fit modelling result for the rock avalanches modelled in full 2.5D is superposed on each map where applicable (black dashed line).

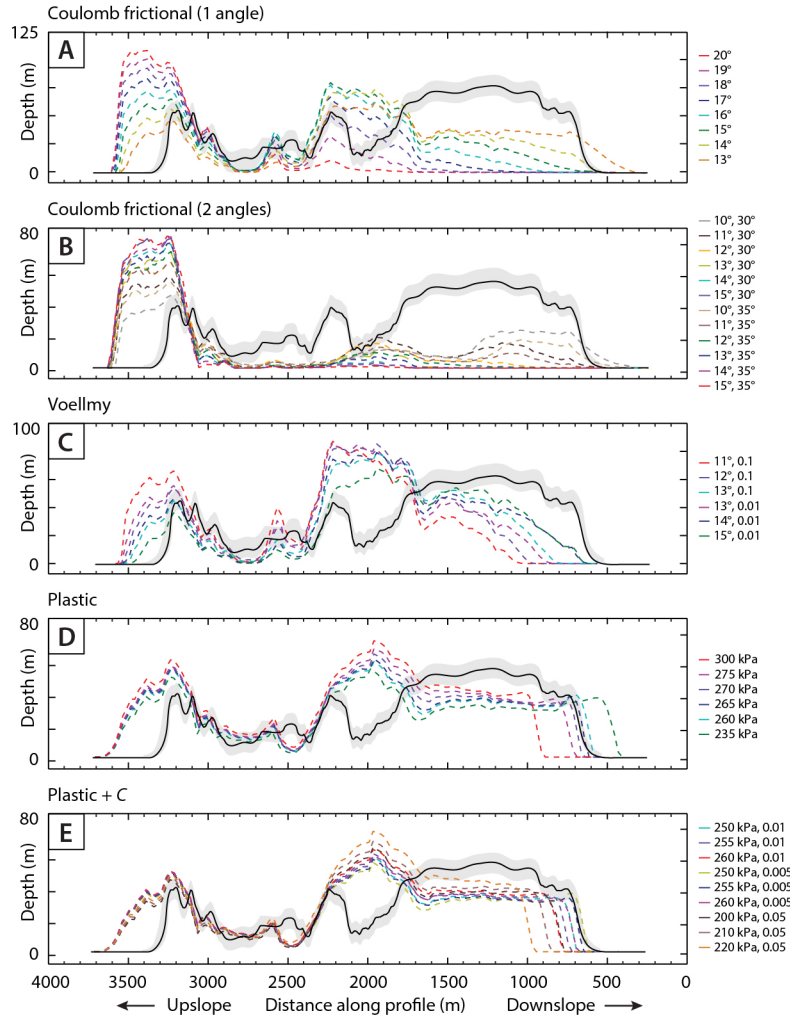


Figure 6. Longitudinal transects through the observed (solid black line) and modelled deposits (coloured lines) of the Paatuut rock avalanche for the frictional rheology (1 and 2 angle), Voellmy rheology, plastic rheology and a plastic rheology with a collisional stress added. The grey shading represents the overall RMS error of the DEM. Transects taken along line A – A' (Figure 4a).

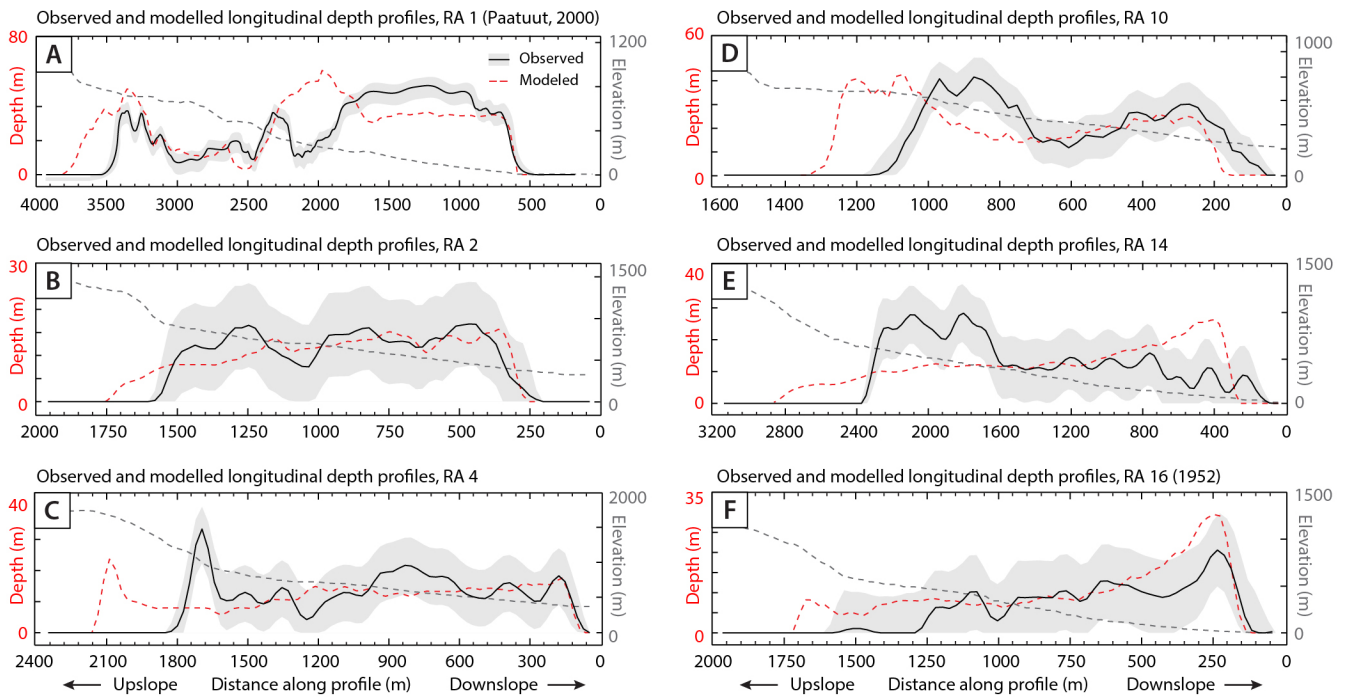


Figure 7. Longitudinal transects through the observed (solid black line) and modelled deposits (dashed red lines) for the six rock avalanches simulated across full 2.5D terrain. The pale grey shading represents the overall RMS error of the GIMP DEM (Howat *et al.*, 2014). The dashed grey line represents the elevation of the path topography.

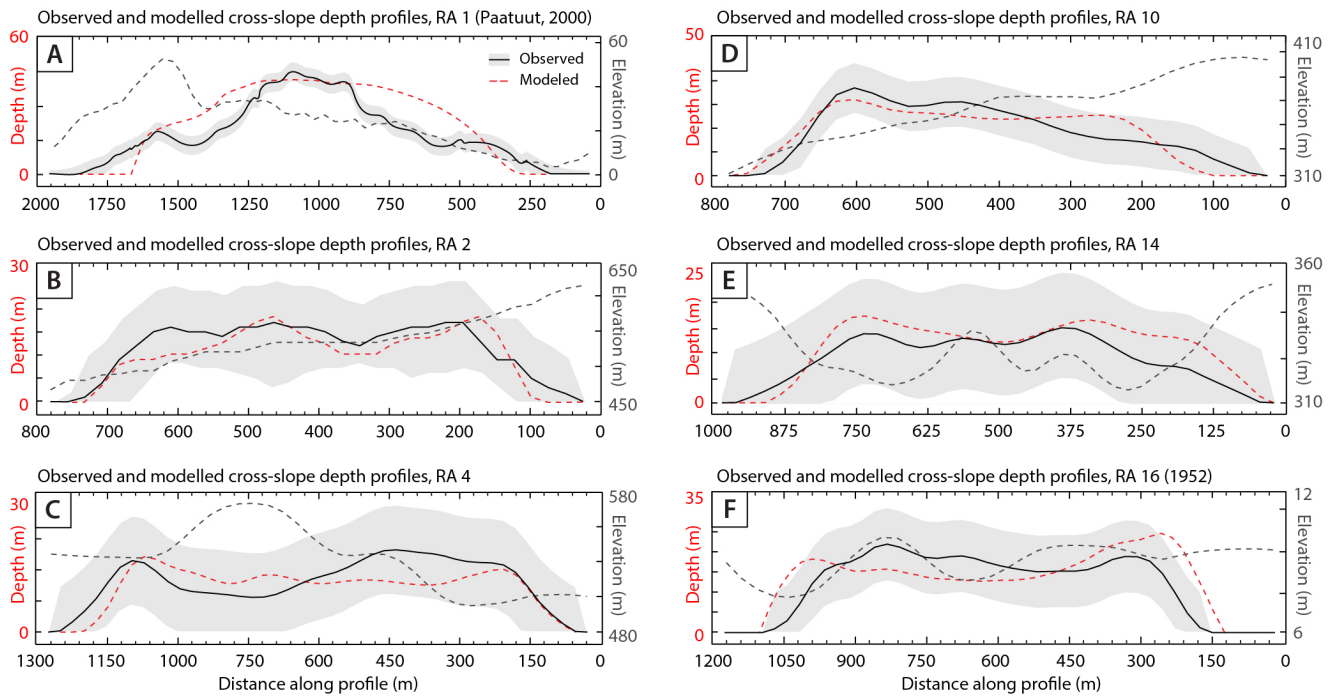


Figure 8. Cross-slope transects through the observed (solid black line) and modelled deposits (dashed red lines) for the six rock avalanches simulated across full 2.5D terrain. Profiles are taken through the toe of the deposit. The pale grey shading represents the overall RMS error of the GIMP DEM (Howat *et al.*, 2014). The dashed grey line represents the elevation of the path topography.

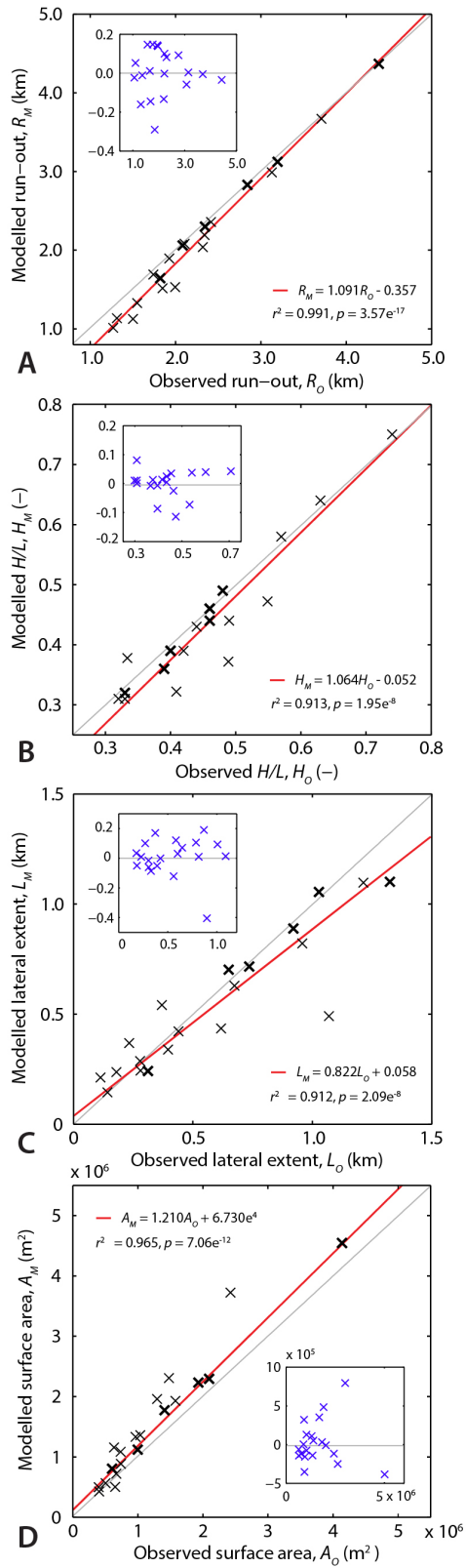


Figure 9. Observed vs. modelled plots of (a) run-out, (b) apparent coefficient of friction, H/L , (c) lateral extent at toe, and (d) depositional area, for all 20 cases. Inset: residual vs. fitted plots for each regression. Markers in bold denote events modelled in full 2.5D.

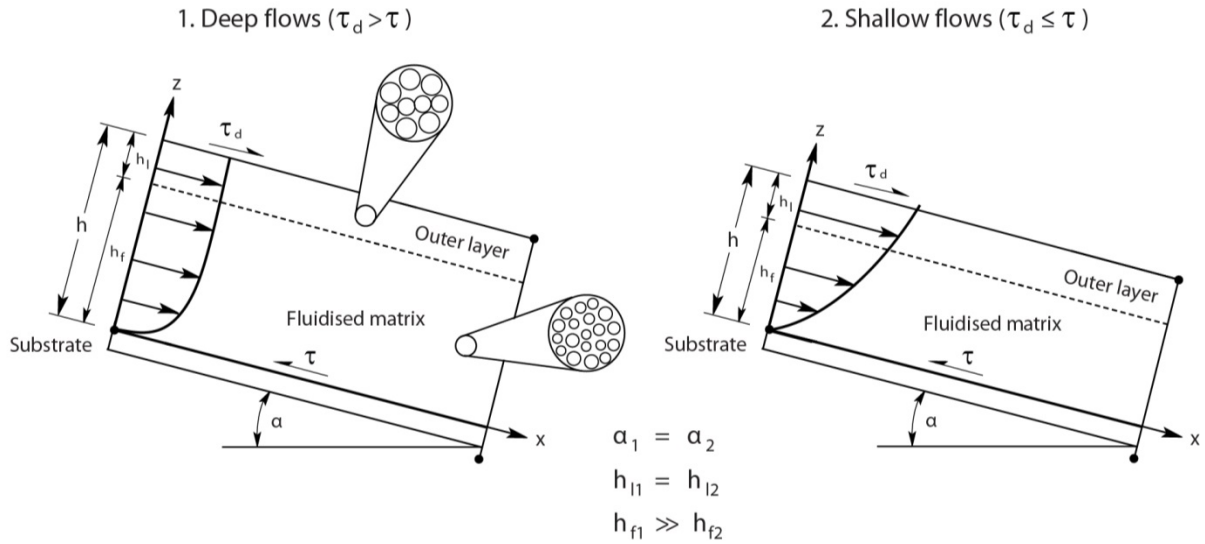


Figure 10. Schematic diagram of the system described in text. Here, rock avalanches are composed of a fluid-like interior of matrix-supported debris (depth = h_f) surrounded by a more resistant outer layer (depth = h_l). In deep flows (1), the low-friction interior in contact with the ground would permit flow even on gentle slopes (small α), with the more frictional outer layer simply being rafted. This would act to prolong flow capability. In shallower flows (2), the influence of the resistant outer layer would increase, reducing the driving stress of the flow (τ_d). Diagrams adapted from the Louge (2003) schematic of steady, fully developed flows down an inclined plane.